

Review

Unconventional methods of imaging: computational microscopy and compact implementations

Euan McLeod¹ and Aydogan Ozcan^{2,3,4,5}¹ College of Optical Sciences, University of Arizona, Tucson, AZ 85721, USA² Department of Electrical Engineering, University of California Los Angeles (UCLA), Los Angeles, CA 90095, USA³ Department of Bioengineering, University of California Los Angeles (UCLA), Los Angeles, CA 90095, USA⁴ California NanoSystems Institute (CNSI), University of California Los Angeles (UCLA), Los Angeles, CA 90095, USA⁵ Department of Surgery, University of California Los Angeles (UCLA), Los Angeles, CA 90095, USAE-mail: ozcan@ucla.edu and euamc@optics.arizona.edu

Received 25 January 2016

Accepted for publication 14 April 2016

Published 23 May 2016



Abstract

In the past two decades or so, there has been a renaissance of optical microscopy research and development. Much work has been done in an effort to improve the resolution and sensitivity of microscopes, while at the same time to introduce new imaging modalities, and make existing imaging systems more efficient and more accessible. In this review, we look at two particular aspects of this renaissance: computational imaging techniques and compact imaging platforms. In many cases, these aspects go hand-in-hand because the use of computational techniques can simplify the demands placed on optical hardware in obtaining a desired imaging performance. In the first main section, we cover lens-based computational imaging, in particular, light-field microscopy, structured illumination, synthetic aperture, Fourier ptychography, and compressive imaging. In the second main section, we review lensfree holographic on-chip imaging, including how images are reconstructed, phase recovery techniques, and integration with smart substrates for more advanced imaging tasks. In the third main section we describe how these and other microscopy modalities have been implemented in compact and field-portable devices, often based around smartphones. Finally, we conclude with some comments about opportunities and demand for better results, and where we believe the field is heading.

Keywords: imaging, computational microscopy, compact implementations, optical microscopy

(Some figures may appear in colour only in the online journal)

1. Introduction

The compound microscope was invented around the year 1600 [1, 2]. Its basic design, fundamentally consisting of a light source, a condenser lens, a sample to be imaged, an objective lens, and an eyepiece, has proven to be highly robust and versatile. The vast majority of microscopy performed today

still relies on these elements and, in particular, the microscope objective lens to form a direct optical image of the sample, be it in pathology imaging for medical diagnoses, in fundamental biological research, or in materials inspection in industrial manufacturing. Of course, as one would expect, many hardware enhancements have been made over the years to the basic microscope design, including additional optical components

and digital cameras that enable imaging modalities beyond brightfield, such as fluorescence, phase contrast, or polarization, among others. In the past decade however, several unconventional methods of imaging have been developed that move away from the paradigm of capturing direct images of the sample using hardware centered around a microscope objective. These new methods have allowed researchers to avoid some of the limitations inherent in the design of the conventional optical microscope.

One such limitation is the trade-off between resolution and field of view (FOV), and it is related to the *space-bandwidth product*, which is proportional to the area of the field of view divided by the area of the smallest resolvable spot. One intuitive way to interpret the space-bandwidth product is as the amount of information captured by the imaging system; the greater the space-bandwidth product, the more information. Another way to interpret it is as the number of pixels necessary on an image sensor for the captured images to be diffraction-limited in resolution and not pixel-limited. For standard research-grade microscopes, the space-bandwidth product for a large range of objectives is on the order of 10^6 – 10^7 , calculated based on the diameter of the FOV, which is equal to the field number of the eyepiece (typically ~ 25 mm) divided by the magnification M of the microscope objective, and the resolution of the system, which is $\Delta x \sim \lambda/(2 \text{NA})$, where λ is the wavelength of the light and NA is the numerical aperture of the microscope objective. To increase the space-bandwidth product of a conventional microscope design, one would need to find an objective with lower magnification and higher NA, however this combination is in opposition to how these two quantities typically scale with respect to each other. Yet it is important to note that this typical scaling and trade-off between NA and magnification is not imposed by a fundamental physical law, and with better lens design it is possible to create objectives that have high NA but low magnification. Examples of such objectives exist through exquisite design and construction: e.g. the objectives used in recent studies of whole-brain imaging had an NA of 0.8 and a magnification of only 16X [3]. However the drawback is that these low-magnification, high-NA objectives tend to be extremely expensive. Thus, it is desirable to find other cost-effective approaches to increase microscopes' space-bandwidth product.

Another conventional microscopy limitation worth highlighting is its limited ability to handle three-dimensional (3D) or optically dense samples. At the minimum, acquiring images of a sample at different depths (called sectioning) requires mechanical refocusing of the imaging system. Furthermore, often simple refocusing alone is not sufficient because the scattering from out-of-focus objects results in artifacts or severe noise in the desired imaging plane. There exist techniques to deal with this issue, such as confocal microscopy [4, 5], or multi-photon microscopy [6–8], however these techniques also require mechanical scanning of the sample or other elements in the optical system and have limited FOVs.

From an ease-of-use standpoint, two other drawbacks of objective-lens based imaging are the bulkiness and cost of the microscopy systems. Imaging platforms with high magnification typically require a long distance, d_i , between the objective

lens and the image sensor, both in older finite-conjugate microscope objectives, as well as in modern infinity-corrected objectives. Objectives with very short focal length, f , could, in principle, solve this problem as $d_i \sim fM$, however manufacturing low-aberration lenses with very small focal lengths is quite challenging and costly, and thus a larger d_i is often chosen.

Here we review several microscopy methods that have emerged in the past decade or so to overcome these limitations by breaking the paradigm of direct imaging via an objective lens or a set of lenses. In section 2, we describe approaches that incorporate computational imaging with existing lens-based microscope systems. In these approaches, the imaging system does not record a direct image of the sample, but rather raw data that can be computationally processed to recover an image. Light-field microscopic imagers, microscopes with active illumination control, and compressed-sensing based microscopes are all examples. Some of these computational imaging approaches extend the space-bandwidth product of the microscope, while others provide the capability to reconstruct 3D volumes of data via computational refocusing. In both cases, there is a push to acquire more and more information about the sample, requiring the acquisition of large amounts of raw data provided by a large number of pixels. As a result, much of this development has been fostered by the exponential growth of pixel counts on charge coupled device (CCD) or complimentary metal-oxide-semiconductor (CMOS) image sensors, similar to Moore's law for the growth of the transistor count on integrated circuits [9–11].

In section 3, we review another family of approaches based on on-chip imaging using lensfree in-line holography [12]. These approaches do away entirely with objective lenses, and thus do not carry the same limitations in space-bandwidth product or device size. The fundamental principle behind these approaches is that a coherent, or partially-coherent, light source is used to illuminate a transmissive sample. The interference between light that passes straight through the sample undisturbed and the light that is scattered off of objects on the sample generates a fringe pattern that can be directly recorded on the image sensor. By computationally back-propagating this recorded fringe pattern, it is possible to reconstruct the original object. Phase recovery techniques can also be combined with these lensfree holographic computational imaging approaches to provide a greater degree of robustness in the samples that can be imaged.

In section 4, we review a host of new devices that have been developed, primarily to reduce the cost and increase the portability and field-use of high-performance microscope systems. In some cases, these operate based on the principles discussed in sections 2 and 3, while in other cases they are particularly ingenious ways of shrinking conventional microscope systems. Often, these portable imaging systems are built around smartphones.

Finally, in section 5, we discuss some of the ways we feel that the field will progress in the coming years. Primarily because they have been reviewed in great detail recently [13–16], in this review we have not discussed localization-based super-resolution approaches, some of which won the

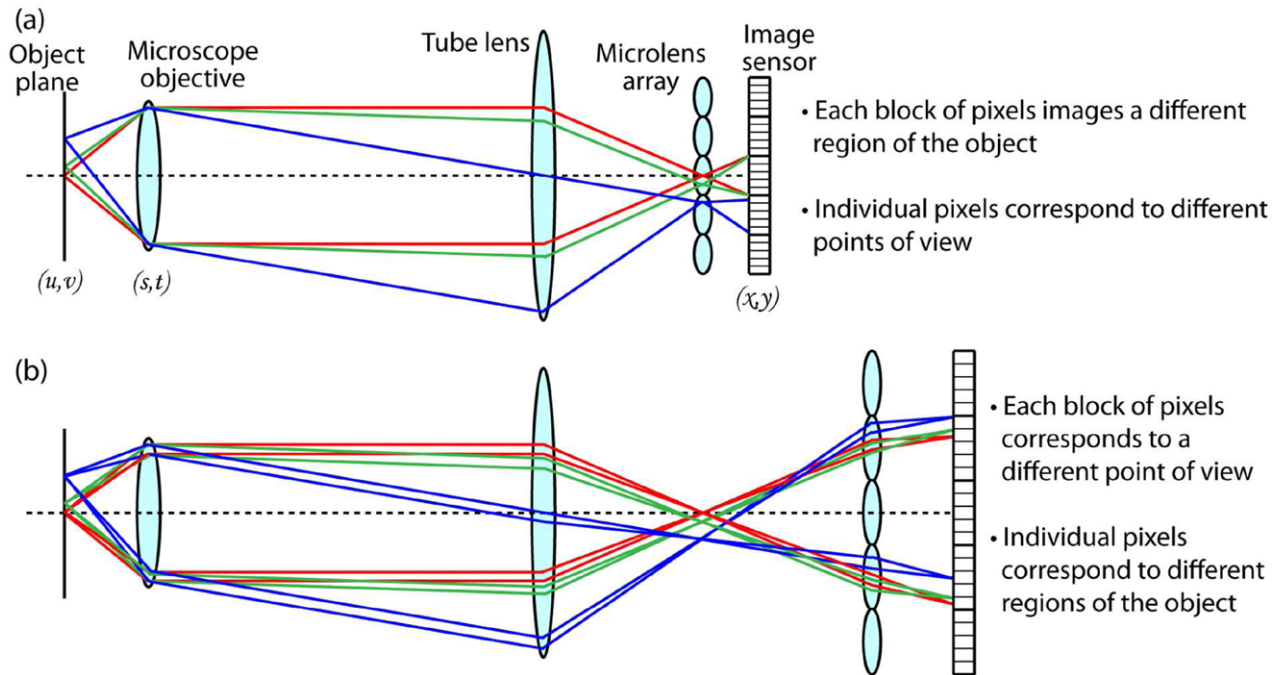


Figure 1. Light field microscopy. Two configurations are shown. (a) A light field microscope where the microlens array is placed at the image plane. (b) A light field microscope where the microlens array is placed beyond the image plane and the image sensor is conjugate to the image plane.

Nobel prize in chemistry in 2014. Super-resolution approaches such as photoactivated localization microscopy (PALM) [17] and stochastic optical reconstruction microscopy (STORM) [18] would otherwise fit within the framework of this review as they are computational imaging approaches that increase resolution, and consequently the space-bandwidth product of microscopy systems.

2. Lens-based computational imaging

2.1. Light-field microscopic imaging

Although existing conceptually for more than a century [19], light-field imaging, also known as integral imaging, has only recently become a particularly attractive option for 3D microscopic imaging. The goal of light-field imaging is to not just capture the intensity of the light across a particular plane in space, but to also capture the direction that the light was travelling to get to that plane. With this information, one can reconstruct what the light would have looked like at other planes in space, i.e. images can be digitally re-focused. As mentioned in the introduction, one of the major advances that has contributed to the recent viability of light-field imaging is the development of image sensors with high pixel counts. A large pixel count is necessary for high-quality light-field reconstructions due to the level of information required to record images across four dimensions compared to that required for two-dimensions.

Light-field imaging is often considered from a geometric optics standpoint where the goal is to capture information about the four-dimensional (4D) light-field. This 4D scalar light-field can be considered a simplified version of the 5D

plenoptic function, which is defined as the radiance of a light ray oriented at a particular angle (θ, ϕ) at a given point in space (x, y, z) . If one assumes that the radiance of the ray does not change as it propagates, i.e. it is neither attenuated nor amplified, then one of the five plenoptic dimensions becomes redundant, leaving four independent dimensions, which constitute the light-field [20]. These four different dimensions can be represented in a variety of ways; one option is to identify each ray by the (x, y) coordinates with which it intersects a given plane, and by the angle of the ray (θ, ϕ) . Another common method of representing these four dimensions is to track the coordinates with which each ray intersects two parallel planes separated in z . These planes are often denoted the (u, v) and (s, t) planes (one example is shown in figure 1(a)). In this representation, the light-field function $L(u, v, s, t)$ describes the radiance of rays in this space. Once the 4D light-field is captured, it can be used to reconstruct images of objects from various perspectives and at various depths, subject to other considerations such as diffraction, resolution, and the numerical apertures of the imaging lenses involved.

In a typical imaging system, only (x, y) information is recorded on CCD or CMOS image sensors, and therefore an appropriate system design is required to correlate recorded information with the correct coordinates in the 4D light-field. One of the most common and simplest approaches is to insert a microlens array into a conventional imaging system in front of the image sensor chip. There are two natural ways to align such a system: one where the microlens array is placed at the image plane and the sensor is placed beyond it at a plane conjugate to the pupil plane, and the other where the microlens array is placed at a plane conjugate to the pupil plane, and the image sensor is placed beyond it at a plane conjugate to the

image plane, as shown in figure 1. In the first case, the raw image would look like a mosaic where the large-scale pattern is an image of the entire sample, whereas in the latter case, the raw image would be an array of small, low pixel count images of the sample, but from slightly different perspectives. Both configurations provide information about the 4D light-field, however the mapping from raw (x, y) pixel locations to (u, v, s, t) coordinates is different (see figure 1). In both cases it is important to design the overall imaging system such that each individual pixel on the sensor is mapped to a unique microlens, in other words, light passing through two different microlenses cannot impinge on the same pixel. Although also commonly used interchangeably, the term ‘integral imaging’ is most often applied to the case shown in figure 1(b) where the microlens array is conjugate to the pupil plane, while the term ‘light-field’ imaging is most often associated with situations where the microlens array is placed at the image plane, as in figure 1(a). Recent implementations of light-field and integral imaging were first performed in macroscopic camera-like imaging systems [21–23], but were quickly adapted for microscope systems. Compared to macroscopic imaging, two unique features of microscopic light-field imaging are that diffraction becomes more significant, and that many objects of interest are partially transparent, which can interfere with the assumptions involved in reducing the 5D plenoptic function to the 4D light-field function; in other words, in addition to diffraction and coherence of light, object dependent shadowing, absorption and scattering events create technical challenges for standard light-field imaging techniques.

One of the earlier papers on light field microscopy was published by Levoy *et al* in 2006 [24]. In addition to showing experimental results, this paper covers in detail the tradeoffs that must be considered when designing a light-field microscope in the configuration shown in figure 1(a), where the microlens array is placed at the image plane. The core tradeoff is that of spatial resolution versus angular resolution of the light-field. The spatial resolution is determined by the microlens pitch, as parallel rays impinging on the lens array generate an array of light spots on the detector with the same pitch as the microlens array. Ultimately, diffraction could also constrain spatial resolution, however in most systems the pitch of the microlens array is much greater than the magnified image of the microscope’s point-spread-function (PSF), and therefore diffraction is not typically the limiting factor. Whereas the spatial resolution is determined by the microlens pitch, the angular resolution is determined by the angular field of view of the imaging system and the number of sensor pixels per microlens. In other words, the number of different angles, or perspectives, that can be recorded is determined by the number of pixels behind each microlens.

In a typical design, there are three key parameters of the microlens array that must be carefully selected: the overall size of the array, the radius of curvature (or focal lengths) of each lenslet, and the lenslet pitch. The overall size of the microlens array should be chosen to (at least) cover the image-side field of view of the microscope. Together, the radius of curvature and lenslet pitch should be chosen such that the

numerical aperture of an individual lenslet matches the image-side numerical aperture of the microscope:

$$NA_{\mu l} = \frac{NA_{obj}}{M}, \quad (1)$$

where $NA_{\mu l}$ is the microlens NA, NA_{obj} is the objective NA, and M is the magnification of the microscope system. By matching the numerical apertures in this way, the subimages projected on the sensor by the microlens array will not overlap, and the total dead zone area between the subimages will be minimized. A measure of the number of different ray angles that can be resolved by each microlens is given by the relative sampling of the image plane compared to the diffraction-limited resolution at that plane. In other words, assuming a sufficiently small pixel size at the imager chip, the number of resolvable angles is given by $N_u = p/(\Delta x M)$, where p is the microlens pitch, Δx is the minimum resolvable feature size of the objective, and M is the magnification of the microscope system. In the system presented by Levoy *et al* [24], they use a system with a $40\times/0.95$ NA microscope objective, and a $125\ \mu\text{m}$ pitch microlens array, which results in a spatial resolution of $125\ \mu\text{m}$ and ~ 12 resolvable angles in each direction. One can see that if they were to choose a larger pitch array, they would sacrifice spatial resolution to achieve greater angular resolution. Eventually the pixel pitch at the image sensor plane and aberrations of the individual lenslets could also limit angular resolution.

Once the 4D light-field is recorded, different types of images of the sample can be computationally reconstructed, such as images of the sample from different angles (perspectives), cross-sections of the sample at different depths, or even 3D virtual displays [25]. There are a few different algorithms that can be used to perform this reconstruction, including limited-angle tomography [26], or 3D deconvolution of a measured 3D PSF [5]. When using these approaches to perform reconstructions of cross sections, the depth of field or axial resolution of a single synthetic cross section can be approximated as [24],

$$D_{cs} \approx \frac{(2 + N_u)\lambda n}{2NA_{obj}^2}, \quad (2)$$

where n is the refractive index of the sample. The total depth over which synthetic cross sections can be reconstructed is $\sim (N_u D_{cs})$.

Compared to traditional brightfield microscopy, brightfield *light-field* microscopy places more stringent requirements on the illumination setup. A traditional brightfield microscope uses Kohler illumination to ensure uniform brightness across the field of view. In a light-field microscope, not only is uniform brightness required for high quality images, but so is a uniform angular distribution of incoming light. (One important exception to this requirement is fluorescence imaging, where the fluorescence emission can be assumed to be isotropic, and independent of the angular distribution of the excitation light.) The use of a diffuser can help to homogenize the angular distribution of the light. For more precise control of the illumination field, a digital light projector and microlens

array can be inserted into the illumination path of the microscope [20]. This combination can be used to both correct for imaging aberrations as well as generate additional imaging modalities such as dark-field imaging, or quasi-dark field imaging where the illumination is performed at high angles that are still within the acceptance cone of the imaging objective lens. One challenge in aligning this system is in calibration, however methods have been developed to perform this calibration automatically through the projection of specific black and white patterns onto the microlens array used in the illumination path.

In comparison to traditional microscopy, one of the most severe limitations of light field microscopy is its reduction in spatial resolution due to the tradeoff with angular resolution; the fact that the range of angles and perspectives is rather limited makes the overall gain in 3D imaging capability of the microscope modest, which unfortunately comes at the cost of substantial resolution loss in addition to experimental and computational complexity. In recent years, several groups have worked on improving spatial resolution through a variety of methods. One method is similar to that used in pixel super-resolution (described in detail in section 3.4), where two images are captured sequentially, but with the microlens array shifted diagonally between the two images [27], or shifting the images using a tilted glass plate that can be inserted into the beam path [28]. Under the assumption that the scene has not changed between the two shifted images, the extra data recorded can be used to synthesize a single high-resolution image where the resolution is improved by a factor of $\sqrt{2}$, assuming that the resolution has been originally limited by the pitch of the lens-array. Alternatively, improved computational methods can be used to perform the 3D deconvolution and image reconstruction with higher resolution. In one case, these methods improved the resolution significantly so that it is only ~ 4 times worse than the diffraction limit of the objective, almost two orders of magnitude better than the lenslet pitch [29]. Interestingly, this approach has one drawback in that it tends to fail due to degeneracy of the measurements in a very narrow region toward the center of the reconstructable range in z ; yet outside of this region it performs well. It is possible to address this deficiency however, by using coded wavefront phase masks, such as a spiral phase mask, between the microscope objective and tube lens [30]. The use of such masks is similar to the approach used in coded aperture photography or computational on-chip microscopy [31, 32]. In these approaches, the relationship between the individual pixels on sensor and the object is typically quite complex (whereas in standard light-field microscopy, each pixel can be matched to a particular ray with a given location and orientation). Nonetheless, with proper calibration such coded aperture approaches are also capable of delivering information about the full 4D light field, although the ‘decoding’ of the information can be more demanding [33].

As described above and shown in figure 1(b), there is another common configuration for light-field/integral-imaging microscopy, where the microlens array is placed conjugate with the pupil plane of the microscope instead of at the image plane [34–36]. In this case, the nature of the tradeoffs

is slightly different than in the previous case shown in figure 1(a). In particular, the number of angles, or viewpoints, is determined by the number of microlenses in the array, whereas the spatial resolution is determined by either the width of a diffraction limited spot projected on the sensor, or the pixel size of the sensor, whichever is smallest. This configuration has the same general limitation as the previous configuration, where spatial resolution has been sacrificed to obtain angular resolution. One way to improve spatial resolution is to recognize that two neighboring elemental images (images produced by neighboring microlenses) share significant redundancy as they are looking at the same object from only very slightly different angles. By computationally exploiting this redundancy, it is possible to improve the spatial resolution of reconstructed images [35].

Another focus of recent work on both types of light field microscopes has been to make them more user-friendly by developing new ways of displaying the 3D information, as well as improving image reconstruction times. One way to display the 3D information is to essentially invert the principle of the light field microscope and to place a microlens after a standard display to project images in a 3D fashion [25, 37, 38]. To speed up reconstruction, several groups have developed real-time reconstruction algorithms and platforms capable of operating at >15 frames per second [34, 38]. Acquisition can also be sped up by using an array of cameras that are each capable of transferring data at high rates [39].

In the past couple years, the use of light-field microscopes has gone beyond the technology and proof-of-concept development to various target-specific applications. One such study focused on the simultaneous whole-animal 3D imaging of neuronal activity [40]. In these experiments, both *Caenorhabditis elegans* and zebrafish were imaged. The reconstructable volume was $700 \mu\text{m} \times 700 \mu\text{m} \times 200 \mu\text{m}$, which could be recorded at frame rates of 20 Hz. For smaller volumes, frame rates up to 50 Hz were possible with spatial resolutions of $1.4 \mu\text{m}$ in x and y and $2.6 \mu\text{m}$ in z , which are sufficient to resolve single neurons. Light-field microscopes have also seen recent application in ultra-cold science. One study used light-field microscopy to obtain 3D images of dilute clouds of fluorescent ^{87}Rb atoms [41]. Additionally, light-field microscopy has been shown to be helpful in optical tweezer systems, where it is important to have visual feedback on the 3D position of optically trapped objects [36].

2.2. Computational imaging via illumination control: structured illumination, synthetic aperture, and Fourier ptychography

While light-field imaging provides an option to gather more spatial information by modifying the imaging side of the beam path in a conventional microscope, another strategy to gather more information is to actively control the illumination. In the previous section, one such example was mentioned as an enhancement to light-field microscopy by designing the illumination light path around a digital light projector and microlens array [20]. Such efforts at sculpting the illumination light path to improve microscopy performance can in general be

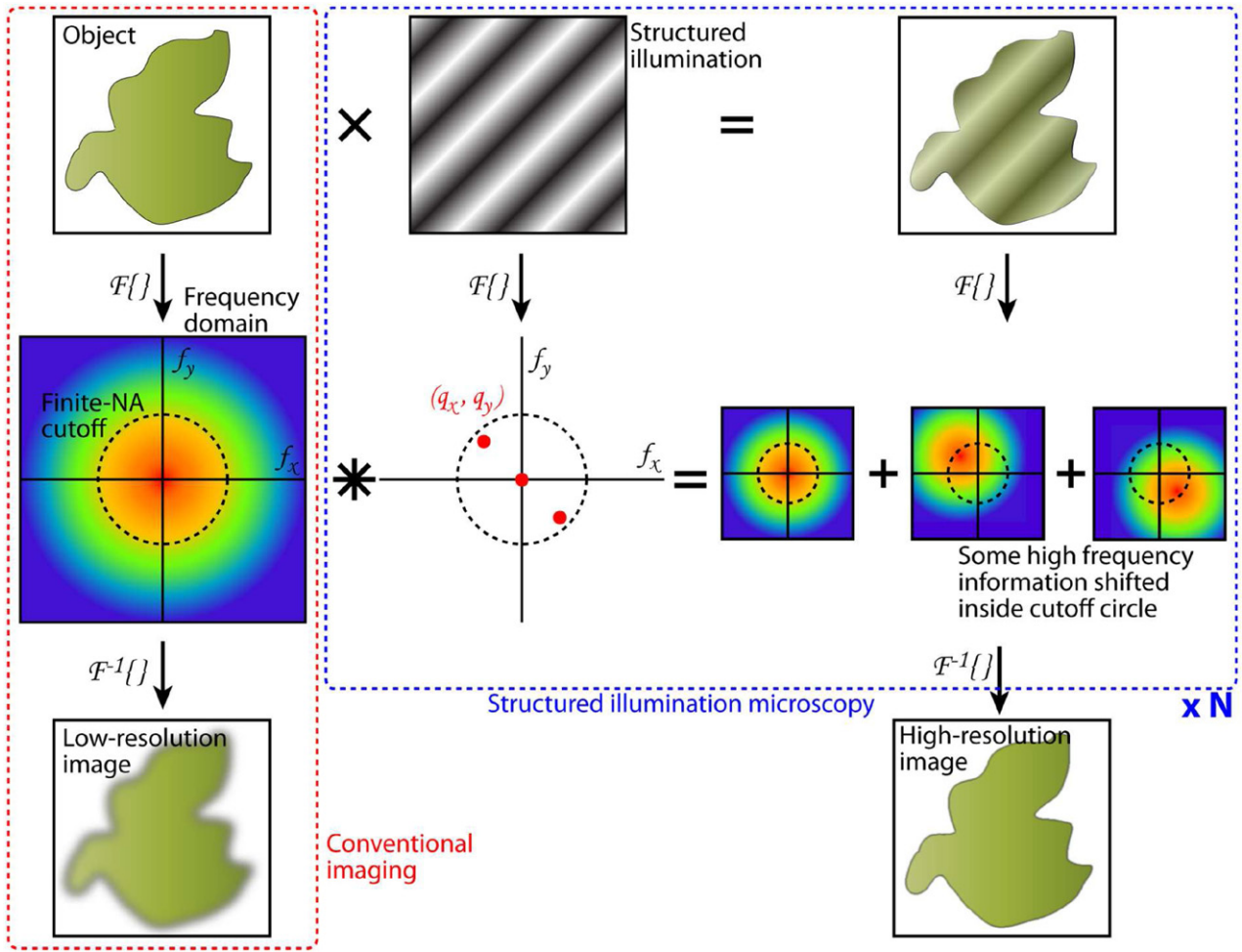


Figure 2. Structured illumination microscopy (SIM). In conventional microscopy, the numerical aperture limits the spatial frequencies transmitted to the image sensor, and thus the resolution of the final image. In SIM, the structured illumination shifts frequencies in the Fourier domain via convolution, allowing high frequency information to pass through the finite NA of the objective. By repeating this process for many different illumination patterns, an image with high resolution in all directions can be reconstructed.

quite powerful, and can lead to many beneficial effects such as improved resolution, increased field of view, and 3D reconstruction capability.

One example of using illumination control to improve resolution is a technique called structured illumination microscopy (SIM) [42, 43]. In SIM, the sample is illuminated with a sinusoidal fringe pattern resulting from the interference between two coherent beams of light, see figure 2. This grating pattern is then shifted across the sample in discrete steps and orientations, and an image is captured after each shift. Thus, many different images are captured for many different combinations of grating orientations and shifts. These images can then be computationally reconstructed into a higher-resolution image than would be possible from a single raw image capture, thereby increasing the space-bandwidth product of the imaging system.

A high-resolution image can be inferred from the recorded images because the known illumination pattern shifts the high spatial frequency content of the unknown sample into low-frequencies, in the same way that two high-frequency patterns overlaid can generate a low beat frequency, also known as a Moiré pattern. Mathematically, this is also the consequence of the fundamental frequency-shifting property of Fourier

transforms. To better formulate and discuss the operation principles of SIM, without loss of generality, let us assume a fluorescence imaging system, where the sample's fluorescence distribution can be denoted by $g(x, y)$. Let the intensity of the structured illumination pattern be defined by the periodic function $\frac{1}{2} [1 + \cos(2\pi(q_x x + q_y y) + \phi)]$, where q_x and q_y represent the periodicities of the pattern in the x and y directions and ϕ describes the spatial shift of the grating pattern. The pattern that is imaged is the spatially modulated sample fluorescence which can be expressed as:

$$\begin{aligned}
 I(x, y) &= g(x, y) \frac{1}{2} [1 + \cos(2\pi(q_x x + q_y y) + \phi)] \\
 &= g(x, y) \left[\frac{1}{2} + \frac{1}{4} e^{i2\pi(q_x x + q_y y) + i\phi} + \frac{1}{4} e^{-i2\pi(q_x x + q_y y) - i\phi} \right].
 \end{aligned}
 \tag{3}$$

Let the Fourier transform of $I(x, y)$ be denoted as $\mathcal{F}\{I(x, y)\} = \hat{I}(f_x, f_y)$, where f_x and f_y are the spatial frequencies of I . As the imaging system is subject to a diffraction limit imposed by its numerical aperture, what is actually observed can be written as,

$$I_{obs}(x, y) \propto \mathcal{F}^{-1} \left\{ \hat{I}(f_x, f_y) H \left(\sqrt{f_x^2 + f_y^2} \right) \right\}, \quad (4)$$

where the function $H(\rho)$ is the optical transfer function (OTF) of the imaging system, and (assuming no aberrations) is given by [44],

$$H(\rho) = \begin{cases} \frac{2}{\pi} \left(\arccos \left(\frac{\rho\lambda}{2NA} \right) - \frac{\rho\lambda}{2NA} \sqrt{1 - \left(\frac{\rho\lambda}{2NA} \right)^2} \right), & \rho < \frac{2NA}{\lambda} \\ 0, & \text{otherwise} \end{cases} \quad (5)$$

Note that optical diffraction implies that no information from spatial frequencies greater than $2NA/\lambda$ can be observed at the far-field, and high frequency information near this cut-off frequency is attenuated by the OTF. In the absence of any structured illumination (i.e. $q_x = q_y = 0$), the observed fluorescence of the sample would therefore be stripped of any spatial frequencies greater than $2NA/\lambda$.

However, with the structured illumination, the frequency-shifting property of the Fourier transform implies:

$$\begin{aligned} \hat{I}(f_x, f_y) &= \frac{1}{2} \hat{g}(f_x, f_y) + \frac{1}{4} e^{i\phi} \hat{g}(f_x - q_x, f_y - q_y) \\ &\quad + \frac{1}{4} e^{-i\phi} \hat{g}(f_x + q_x, f_y + q_y), \end{aligned} \quad (6)$$

meaning that the detected spatial frequencies form a superposition of the natural spatial frequencies of the fluorescence distribution ($\hat{g}(f_x, f_y)$) along with its frequency-shifted copies. As a result, the retained spatial frequencies after observation now also include those that satisfy $(f_x - q_x)^2 + (f_y - q_y)^2 < \left(\frac{2NA}{\lambda} \right)^2$ or $(f_x + q_x)^2 + (f_y + q_y)^2 < \left(\frac{2NA}{\lambda} \right)^2$. These relations define two circles in frequency space with the same radius as the original cutoff implied by the diffraction limit, but with the circle centers shifted to (q_x, q_y) and $(-q_x, -q_y)$ instead of $(0, 0)$. Thus, the boundaries of these circles partly extend beyond the original diffraction limit imposed on g , and high spatial frequency information regarding g can now be captured. The relative frequency-space contributions from the three different terms in (6) can be determined by capturing multiple images with different values of ϕ and e.g. solving a set of linear equations. Ultimately, a large frequency-space representation of g that extends beyond the original OTF-induced limit on \hat{g} can be computationally generated using many images captured from various illumination patterns. Finally, this frequency-domain representation is inverse Fourier transformed to yield a high-resolution image of g . If we assume the same type of lens is used to both generate the structured illumination and capture raw images, then the resolution is at most increased by a factor of 2 because we are limited by $q_x^2 + q_y^2 < \left(\frac{2NA}{\lambda} \right)^2$, since the structured illumination pattern is itself generated by a diffraction-limited imaging system.

SIM and variants of SIM have been used and further developed in a large number of studies [45], more than we could possibly cite, although we highlight a few of the more notable examples here. One such example involves combining SIM

with nonlinear fluorescence microscopy to achieve resolutions $< 50\text{nm}$ using visible light [46]. In this approach, the nonlinearity induces higher-order harmonics into the structured illumination pattern with spatial frequencies beyond the standard diffraction limit, so that the limit $q_x^2 + q_y^2 < \left(\frac{2NA}{\lambda} \right)^2$ no longer applies. In other studies, SIM has been combined with other microscopy techniques such as total internal reflection fluorescence microscopy (TIRF), and optical localization microscopy to achieve high sensitivity and resolution [47]. SIM has also been used with nonlinear light sheet microscopy to provide enhanced resolution (at the single-cell level) with 3D imaging of a volume of e.g. $\sim 600\ \mu\text{m} \times 600\ \mu\text{m} \times 200\ \mu\text{m}$ [48]. Recently, SIM has developed to the point where imaging fast processes in living cells with sub-100nm resolution is possible through the minimization of optical power dosage and maximizing frame rates [47, 49].

A different illumination control technique is synthetic aperture microscopy (SAM) [50–54]. As in SIM, and virtually all computational imaging approaches, SAM involves the capture of many images sequentially with the assumption that the sample has not significantly changed during the image capture time. Mathematically, SAM is also similar to SIM, as it involves increasing the area of coverage in the frequency domain before transforming back to the spatial domain with enhanced resolution. However the practical implementation is somewhat different. Whereas SIM projects various intensity gratings onto the sample, SAM projects a uniform plane-wave illumination, but one that comes from different well-defined angles with respect to the sample. In addition, SAM only works with coherent, brightfield diffractive imaging, and not with fluorescence modalities as was the case with SIM.

To better explore the operation principles of SAM, let us assume that the complex transmissivity of the object is denoted with $t(x, y)$. When illuminated with a plane wave at an oblique angle of incidence, the transmitted *field* is,

$$U(x, y) = t(x, y) e^{i2\pi (q_x x + q_y y)}, \quad (7)$$

where q_x and q_y depend on the angle of incidence. Despite significant physical differences between SIM and SAM, the mathematical process of reconstruction is quite similar: in the Fourier domain, the individual images are computationally shifted from the origin by q_x and q_y , and acquiring a sufficient number of images stitched together makes it possible to span a large region in the Fourier domain, which provides higher resolution when transformed back to the spatial domain at the object plane. Another significant difference is that whereas for SIM, the initial transform to the Fourier domain is typically performed computationally, in SAM the Fourier transform can also be performed optically by placing the object at the front focal plane of the microscope objective and the image sensor at the back focal plane of the microscope objective. With SAM, it is also necessary to measure the phase of the light and not just its intensity. To do this, one can use e.g. iterative phase recovery [55, 56] or interfere the light coming from the sample with a known reference beam, similar to holographic microscopy (see section 3) or interferometric microscopy [51, 53, 57].

In one example of SAM, the resolution of 170–180 nm features was demonstrated at a wavelength of 633 nm, using a 0.4 NA lens [54]. This represents a ~ 5 -fold improvement in resolution compared to conventional imaging with the same lens system, and the resolution of features smaller than $\lambda/3$. As SAM at most doubles the diameter of the region in Fourier space accessible to propagating waves, the theoretical resolution limit using high-NA objectives (in air) would be $\sim \lambda/4$. In another application of SAM, tissue slices were imaged with a resolution of 0.6 μm across a field of view of 9 mm² [58], demonstrating simultaneous high resolution and large FOV. Recent efforts in SAM have involved finding ways to increase the acquisition speed, as many images need to be captured to yield a reconstruction. Kim *et al* have developed a high-speed system that can acquire 361 images from different angles using galvanometric scanning mirrors in less than 1/13th of a second [59].

In addition to providing higher resolution and higher space bandwidth products, another advantage of SAM is that since it measures the phase of the light coming from the object, it is capable of generating 3D reconstructions [52], as was also possible using light field microscopy. With both amplitude and phase information, the light can be back-propagated arbitrarily to computationally refocus on any plane in the sample. Ralston *et al* showed reconstructions of tissue slices at different planes spanning ~ 1 mm in z [52].

SAM can also be combined with holography [60–65], which is another technique that makes use of phase information. In lens-based holographic microscopy, the synthetic aperture approach has been used to boost the resolution by a factor of 3 using a $5 \times /0.1$ NA objective lens [61]. In another study, a lens-based holographic microscopy setup was used to provide a resolution equivalent to that of a 0.61 NA objective, corresponding to a resolution of ~ 0.5 μm at a wavelength of 632 nm, but covering an area of ~ 8.4 mm², thus yielding a space-bandwidth product of ~ 134 million [63]. In one lensless approach (see section 3.7 for the description of another lensless synthetic aperture approach [56]), a linear CCD was placed so that it is recording in the Fourier, or frequency domain, and is scanned to record an enlarged area, which translates into increased resolution and space-bandwidth product [62]. In this study, the FOV was 12.25 cm², and the resolution was 2.57 μm , corresponding to a space-bandwidth product of ~ 740 million. Systems such as these have also been applied to imaging biological tissue [58]. Varying tilts of the reference arm can also be used to fill up the Fourier space via synthetic aperture holography [64]. Similar approaches have been also been used in larger-scale imaging tasks to generate synthetic apertures as large as 87 mm \times 129 mm with a resolution of ~ 15 μm [65]. Here, although the resolution is not particularly fine, the overall space-bandwidth product is still quite large.

More recently a derivative of the synthetic aperture idea has been demonstrated which is termed as Fourier ptychographic microscopy (FPM) [66]. This is a brightfield imaging approach, which again uses images generated from illumination at different angles to create an image with enhanced space-bandwidth product. However in contrast to mainstream SAM approaches, the phase is inferred through an iterative

phase-recovery approach (see section 3 for more discussion on phase recovery techniques in general and lensfree implementations of similar ideas). In a typical FPM setup, a low-magnification, low-NA microscope objective is used to provide a large field of view, while higher resolution is achieved computationally. For example, with this approach it is possible to construct a system with 0.78 μm half-pitch resolution across a field of view as large as 120 mm². In an FPM system, the condenser of a conventional microscope is replaced with a 2D array of light-emitting diodes (LEDs). Each LED in the array is turned on sequentially, and an image is captured for each LED. These individual images are inherently low resolution due to the low NA of the microscope objective, but can be combined into a single high-resolution image. This combining process proceeds as follows. First, an initial guess of the high-resolution image is made by simply up-sampling the low resolution image acquired with normal incidence illumination, generated by an LED at the center of the array. An arbitrary phase is also ascribed to the light at the image plane, e.g. $\phi = 0$ uniformly across the field of view. Next this complex function is brought into the frequency domain via an FFT. This function will be dynamically and iteratively updated in the frequency domain in the following steps to converge on a high-resolution image of the real sample. To begin this iterative procedure, an oblique illumination angle is selected, and its corresponding components are extracted from the upsampled frequency domain image that was computed for normal illumination. These corresponding components are the values that lie within a circle in the frequency domain whose center is determined by the incidence angle of the illumination and whose diameter is determined by the NA of the objective. Based only on those extracted components, a low resolution image corresponding to that illumination angle is computationally synthesized through an inverse Fourier transform. At this point, the direct measurement of the image corresponding to this angle is used by replacing the amplitude of the computationally-synthesized image with the measured one. The phase of the computationally-synthesized image is left untouched. This updated computational image is then transformed back to the frequency domain, and the corresponding components are updated in the upsampled image that is being dynamically updated. These steps are performed for each acquired illumination angle, and the entire cycle is then repeated again another 1–2 times to attain reasonable convergence. Finally, the upsampled Fourier domain image is restored to the spatial domain through an inverse Fourier transform, yielding high-resolution intensity and phase images across a large field of view.

Although it only relies on intensity measurements, FPM still assumes a coherent imaging system provided by small-aperture monochromatic or quasi-monochromatic light sources positioned far from the object (see section 3.1 for a discussion on coherence). Thus, this technique is not compatible with fluorescent imaging approaches. Another central challenge in FPM is the calibration of the illumination angles. Precise knowledge of these angles is essential for the iterative reconstruction procedure to converge successfully.

Several studies have gone on to make improvements over the basic FPM setup. One class of improvements has made

FPM more efficient in terms of data capture and processing. By reducing the number of raw images necessary, total image acquisition time can also be reduced. One way to accomplish this is by skipping angles that are unlikely to provide much additional information (based on a preliminary low-resolution analysis of the sample). With this method, it is possible to reduce the number of images by $\sim 70\%$ without significantly degrading the final image quality [67]. In another approach, Tian *et al* note that it is possible to activate several LEDs simultaneously, as long as they are well separated in angle, without significantly degrading performance [68]. This is possible because these different LEDs cover different regions in frequency space and do not interfere with each other. As a result, the number of raw images can be reduced by approximately a factor of 10. The reconstruction algorithms themselves have also been improved to become more robust, more accurate, faster, and more efficient [69].

FPM has also been adapted to handle more challenging samples, such as those with a degree of thickness [70], or those undergoing motion [71]. In the latter case, a long camera exposure time is used such that multiple LEDs will be switched on and off in a single image. When the activation timing of the different light sources are known precisely, the motion of the object is encoded in the different illumination angles from different LEDs. This information can be decoded from within the frequency domain.

FPM has also been extended to include multiple imaging modalities. As noted above, the fundamental FPM setup requires a coherent imaging system. Within these guidelines, FPM can be used to generate brightfield, darkfield, and quantitative phase contrast reconstruction images, all from the same set of initial data [72, 73]. These different modalities lend themselves to different types of applications depending on the specimens being imaged. The combination of FPM with integral imaging using a microlens array has also been proposed and tested [74].

In addition to structuring of illumination and synthetic aperture ideas to compute microscopic images with large space-bandwidth products, recent work has also shown the use of the diversity of illumination wavelength (over a narrow spectral range of $\sim 10\text{--}30\text{nm}$) to significantly improve the resolving capabilities of pixelated (or under-sampled) lens-based imaging systems [75]. The same framework has also been used to improve the resolution of lensfree on-chip microscopy, which will be further discussed in section 3.

2.3. Compressive imaging

Compressive imaging refers to a specific set of applications based on the more general concept of compressive sensing or sampling. Compressive sensing/sampling [76–79] is a family of approaches by which accurate reconstructions of signals are possible with fewer measurements, or samples, than would typically be expected using conventional sampling theory based on the Nyquist–Shannon sampling theorem. In other words, under certain constraints it is possible to reconstruct a discrete signal with a sampling rate less than twice the maximum frequency of the signal. The two requirements

of compressive sensing are (1) that the signal is sparse when transformed into an appropriate basis (such a basis can be found for most real-world signals, with the wavelet basis being one of the most notable for typical photographic data [80, 81]), and (2) that the apparatus used to make the measurements should inherently measure the signal in a basis that is uncorrelated, or incoherent, with the basis where the signals are sparse. Note that the use of ‘incoherence’ in this section does not refer to incoherent light, but rather a mathematical definition of incoherence [79].

Mathematically, we will assume that we wish to acquire or reconstruct a discrete signal f of length n from m independent single-valued measurements. For example, this could correspond to the reconstruction of an image discretized as an array of n pixels, from an image captured using m independent measurements or pixels. Due to the complexity or cost of making many measurements, we assume it is desirable to completely reconstruct f without having to measure each of its n components individually, i.e. we want to find a reconstruction procedure even when $m < n$.

It is important to note that for many measurement systems, the signal of interest is not directly sampled by raw measurements, but instead a transformed signal is sampled, for example in Fourier transform infrared (FTIR) spectrometers, Fourier plane imaging microscopy, or holography. To account for such modes of measurement, we therefore assume that the raw measurements are,

$$y_k = f \cdot \phi_k, \quad k = 1 \dots m \quad (8)$$

or equivalently,

$$y = \Phi_{\text{subset}} f, \quad (9)$$

where the ϕ_k are a subset of a set of orthonormal basis vectors, and $\Phi_{\text{subset}} = [\phi_1 \dots \phi_m]$ is an $n \times m$ matrix, where the columns are a subset (not necessarily densely packed) of $\Phi = [\phi_1 \dots \phi_n]$, which is an $n \times n$ matrix. For example, these basis vectors could represent Fourier modes of different frequencies. In principle it seems as if the reconstruction of f is as simple as the (pseudo-)inversion of equation (9). However, because Φ_{subset} is not full rank due to the limited number of measurements, there is not a unique solution to this problem through simple inversion, and in general many solutions exist. A compressive sensing/sampling framework allows one to find the correct solution, given some assumptions. Before defining these assumptions, let us express f in terms of another basis Ψ ,

$$f = \sum_{i=1}^n x_i \psi_i, \quad (10)$$

or equivalently,

$$f = \Psi x, \quad (11)$$

where the ψ_i constitute a *full set* of orthonormal basis vectors and therefore $\Psi = [\psi_1 \dots \psi_n]$ is an $n \times n$ matrix.

The main result from compressive sensing is that f can be computationally reconstructed *exactly* by \hat{f} (i.e. $\hat{f} = f$ with ‘overwhelming probability’ [79]) from the set of measurements y_k using the equation,

$$\hat{f} = \Psi \hat{x}, \quad (12)$$

where,

$$\hat{x} = \underset{x \in \mathbb{R}^n}{\operatorname{argmin}} \|x\|_{\ell_1} \text{ subject to } y_k = \langle \Psi x, \phi_k \rangle \text{ for all } k = 1 \dots m, \quad (13)$$

and ℓ_1 denotes the use of the ℓ_1 norm:

$$x_{\ell_1} = \sum_{i=1}^n |x_i|, \quad (14)$$

with the further condition that the number of measurements m is sufficiently large, satisfying

$$m \geq C \mu^2(\Phi, \Psi) S \log n, \quad (15)$$

where C is a positive constant, $\mu(\Phi, \Psi)$ is the coherence of the two bases, defined as

$$\mu(\Phi, \Psi) = \sqrt{n} \max_{1 \leq k, j \leq n} |\phi_k, \psi_j|, \quad (16)$$

and S is a measure of the sparsity of the signal f expressed in the Ψ basis, equivalent to the number of nonzero elements of x in equation (12).

The implementation of a successful compressive sensing approach is benefited by several key observations. First, the computationally challenging step in performing the reconstruction is contained in equation (13), yet problems in this form are tractable and have been well studied and can be solved via linear programming algorithms [82]. Second, the two assumptions of sparsity and incoherence are incorporated together in equation (15), where one concludes that if the signal is sparser or the two bases are less coherent, then fewer measurements are necessary for exact reconstruction. Third, while each measurement should correspond to a different basis vector from Φ , it does not matter which specific basis vectors are used, provided that enough are chosen to satisfy equation (15), and in fact, these basis vectors could be chosen completely randomly regardless of the nature of the signal f .

The analysis presented above forms only a bare-bones introduction to compressive sensing. Reference [79] provides a more comprehensive introduction, discussing how these approaches perform in the presence of noise, how to best select the bases Φ and Ψ , and how well compressive sensing performs for signals that are not exactly sparse, but have many components that are near zero in the appropriate basis, and thus could be neglected. It turns out that a good rule of thumb is that when the two bases are chosen appropriately, it is practically possible to obtain an exact reconstruction for $m \sim n/4$ [83].

One of the first imaging applications of compressive sensing to be explored is known as the single-pixel camera [84, 85]. In this experiment, a single pixel, e.g. a photodiode, captures m measurements of an unchanging scene over some time period. Between each measurement, a different mask is introduced in front of the single-pixel detector that modulates the light traveling from the scene to the detector. In the notation above, each mask corresponds to a different ϕ_k . A convenient way of generating these masks is to use a spatial light modulator such as a digital micromirror device (DMD) where each micro-mirror pixel is binary, and can be set to either reflect the

image toward the sensor or away from the sensor. A particular ϕ_k then corresponds to a particular pixel pattern on the DMD. The patterns can either be chosen randomly (which works quite well), or they can be chosen from a known basis such as noiselets that are rather incoherent with wavelets, which form a common sparsifying basis for photographic images [86].

Beyond general imaging, compressive sensing has been applied to several microscopy applications. In one case, the single-pixel camera approach was integrated with a microscope system to enhance its 3D sectioning capabilities [87]. Standard brightfield microscopes have limited sectioning capability because scattering from out-of-focus objects can severely corrupt measurements at the desired plane (section). One common solution to this problem is to use confocal scanning where a pinhole is placed at the image plane to reject out of focus light [88]. However, acquiring sections in this manner requires scanning a focal spot throughout the entire sample, which can take considerable time. Instead, compressive sensing can be used to significantly reduce the data acquisition time by replacing the pinhole near the detector in a confocal microscope system with a random mask implemented using a digital micro-mirror device (similar to the single-pixel camera idea). Similar approaches can be applied to virtually any scanning-based microscopy technique, with another specific example being nonlinear microscopy [89].

Compressive sensing has been combined with other high-resolution fluorescence microscopy techniques like the localization microscopies, PALM [17] or STORM [18]. The benefit of applying compressive sensing techniques to these imaging modalities is that image acquisition times can be significantly sped up by increasing the amount of emitters that are activated simultaneously in a single raw frame. The assumption of sparsity allows one to generate high-resolution images even when the PSFs resulting from multiple emitters are spatially overlapping in the same frame, with emitter densities up to 10 per μm^2 [90, 91].

Fluorescence microscopy in general can also benefit from compressive sensing. Compressive sensing can reduce the number of measurements necessary to accurately capture an image of the sample and can aid in the acquisition of hyperspectral data regarding the fluorescence emission [92]. For *lensless* fluorescence and incoherent microscopy (see section 3), a compressive sensing framework has also helped to improve imaging performance [31, 32, 93, 94], and these applications will be discussed in more detail in sections 3 and 4. Additionally, compressive sensing has been used in fluorescence lifetime imaging microscopy to obtain better measurements of the distribution of fluorophore lifetimes [95].

Another microscopy modality to which compressive sensing has been applied is holographic microscopy. Following in the footsteps of its initial application to macroscopic holography and holography in general [96–106], compressive sensing was used in lens-based holographic microscopy, where little loss in image quality was observed when using as few as 7% of the available detector pixels [107]. In this scheme, the sensing basis was in the Fourier domain where the captured hologram was related to the object through a Fresnel transform. The objects were assumed to have sparse spatial

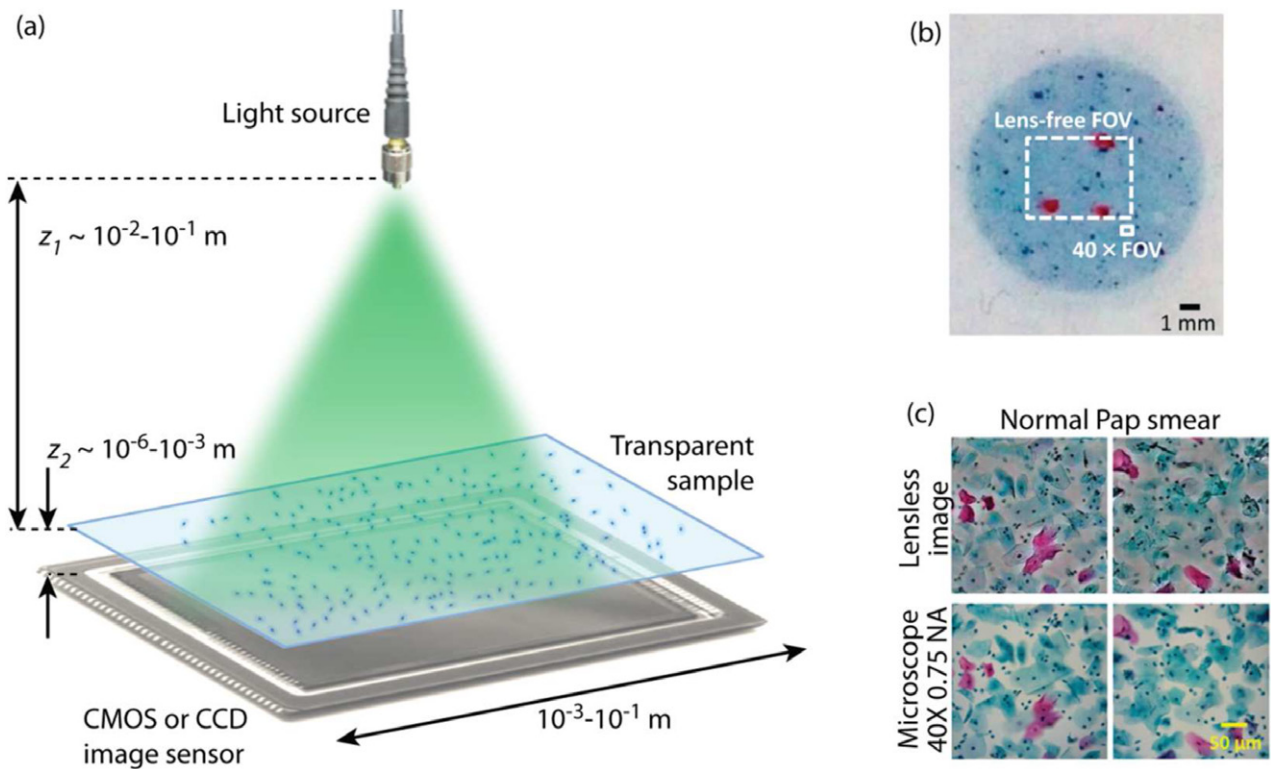


Figure 3. Lensfree imaging. (a) Basic lensfree imaging setup. A partially coherent light source such as an LED directed through a multimode optical fiber illuminates a transparent sample. Diffraction, or interference, patterns are imaged on the image sensor. (b) Lensfree imaging is capable of imaging fields of view much larger than those through a conventional 40X objective, at similar resolution. (c) Lensfree images reconstructed via phase recovery (section 3.7) yield high quality images comparable to conventional microscopes. Panels (b) and (c) are reproduced from [198], copyright 2014 AAAS.

gradients in intensity, which defined the sparsifying basis. Such an approach with the same choice of bases can also be used to generate improved 3D tomographic reconstructions in microscopy at high frame rate [108, 109].

Finally, compressive sensing has been applied to a number of other microscopic imaging modalities. One example is spectral domain optical coherence tomography. Here, it was found that using compressive sensing approaches, the number of pixels required on the image sensor could be reduced by 62.5% while still maintaining accurate and high-resolution images [110]. Here the pixel reduction was performed by zeroing a specified number of pixels, whose locations were chosen randomly. It is also possible to combine compressive sensing with many of the approaches presented in section 2; for example, compressive light field imaging has also been explored [111].

3. Lensfree computational imaging on a chip

Many of the advantages of computational imaging systems discussed in earlier sections are also achieved by lensfree holographic computational imaging on a chip, where the sample is closely placed on the active area of an imager chip, typically with <1 mm vertical gap (see figure 3). These advantages are namely the ability to yield images with large space-bandwidth products, the ability to reconstruct 3D volumes, as well as the ability to recover the phase of objects of interest. Furthermore, in lensless holographic microscopy that is implemented on a chip, the elimination of the objective lens from the imaging

system provides a way to decouple resolution and field view, as in these systems, resolution is primarily influenced by the effective pixel size, while field of view is determined by the size or active area of the image sensor.

In lensless holographic microscopy, the recorded spatial information is the interference between a reference light wave of known properties (this is the light wave passing through the transparent sample substrate unperturbed), and the light wave that has been scattered by unknown objects. From the interference pattern generated by these two waves, the optical properties of the unknown object can be inferred. Unlike other forms of holography, the reference wave here is ‘in-line’ with the scattered wave [112].

3.1. Coherence requirements

As the ability to reconstruct the object depends on the formation of an interference pattern on the sensor, it is necessary that the reference wave and the object wave be coherent with each other, at least to some degree. For partially coherent light, the degree of coherence can limit the resolution because the information from high spatial frequencies is recorded in the smallest fringes at the far extents of the interference pattern (see figure 4(b)). It is therefore important that these fringes be visible in order to yield a high-resolution reconstruction. In comparing the resolution of lensfree imaging systems to those of lens-based imaging systems, the numerical aperture of the lensfree imaging system can be defined based upon the

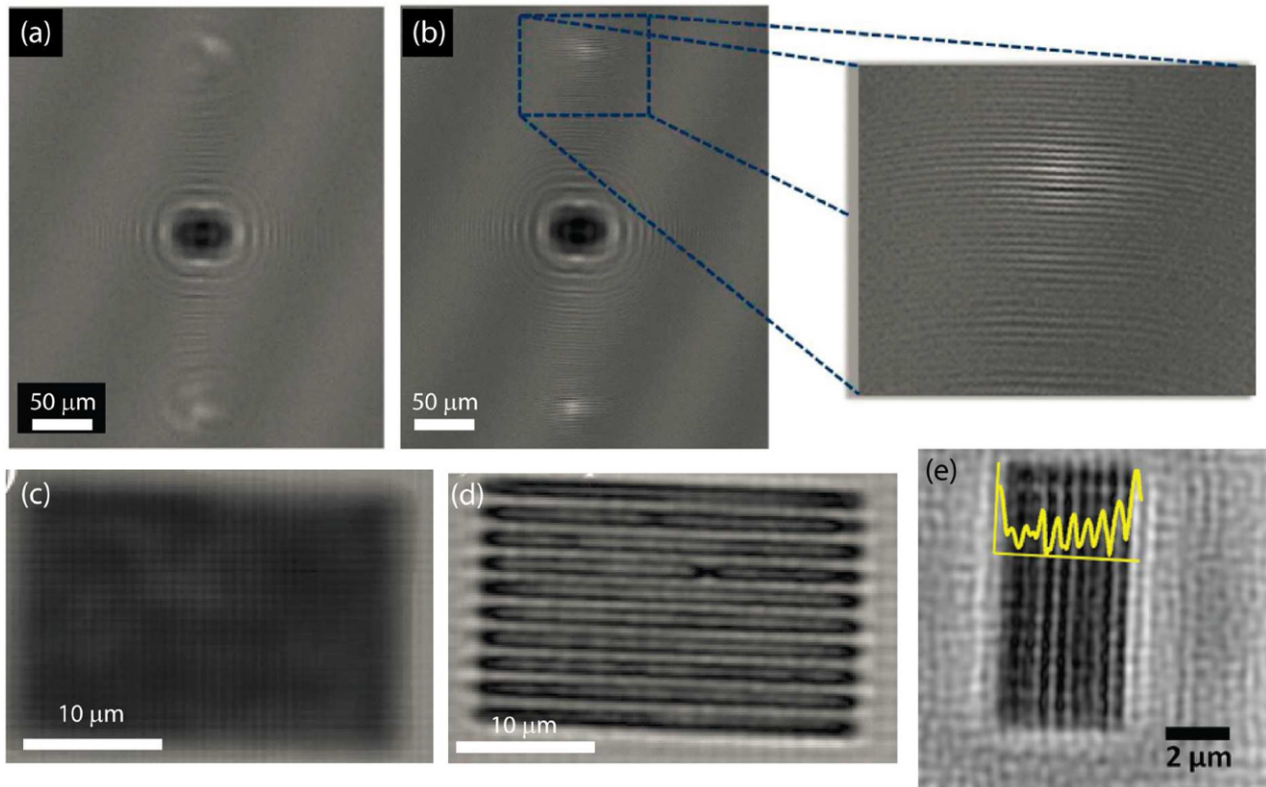


Figure 4. Lensfree holograms and reconstructions. (a) Raw hologram captured where the object is a grating with $1 \mu\text{m}$ half-pitch. (b) Pixel-super-resolved hologram where high frequency fringes are resolved as shown in the inset. (c) Reconstruction from the single low-resolution hologram in (a). The grating lines are not resolved. (d) Reconstruction from the pixel-super-resolved hologram in (b). The grating lines are now clearly resolved. (e) Lensfree holographic reconstruction of an even finer grating with 225 nm half pitch. Panels (a)–(d) are reproduced from [161], copyright 2010 OSA. Panel (e) is reproduced from [164], copyright 2013 Nature Publishing Group.

greatest angle θ_{max} from which scattered light interferes with the plane wave illumination to produce visible fringes. The resulting spatial resolution can then be approximated as,

$$\Delta x \sim \frac{\lambda}{2 \text{NA}} = \frac{\lambda}{2n \sin \theta_{\text{max}}}, \quad (17)$$

where n is the refractive index of the material between the sample and the sensor.

The fringe visibility and maximum scattering angle may be limited by the temporal and/or the spatial coherence of the imaging system. Temporal coherence is often characterized by a coherence length L_{coh} , which represents the distance a beam can travel before its coherence is lost due to the beam containing a spectrum of wavelengths. This length is given by [113],

$$L_{\text{coh}} = \left(\frac{2 \ln 2}{\pi} \right) \frac{\lambda^2}{n \Delta \lambda}, \quad (18)$$

where λ is the central wavelength of the spectrum and $\Delta \lambda$ is the bandwidth of the spectrum. The maximum angle of fringe visibility is determined by when the path length difference between a ray in the reference in-line plane wave and a ray scattered by the object is equal to the coherence length:

$$\theta_{\text{max}} \leq \arccos \left(\frac{z_2}{z_2 + L_{\text{coh}}} \right), \quad (19)$$

This relationship, when combined with equation (17), describes the effective numerical aperture ($n \sin \theta_{\text{max}}$) and the resolution limit imposed by the temporal coherence of the light source.

The spatial coherence imposes its own limitation on resolution as well. If we assume the light source is inherently spatially incoherent (e.g. an LED), then the spatial coherence of the imaging system is determined by the diameter of the light source aperture (D), as well the distance between it and the sample (z_1). Light scattered by the object will be coherent with the incident reference within a cylinder centered at the object with a diameter equal to the distance to the first zero of the complex coherence factor of the light source [113],

$$d_0 = 1.22 \frac{\lambda z_1}{D}. \quad (20)$$

The corresponding maximum scattering angle determined by spatial coherence requirement can then be computed by,

$$\theta_{\text{max}} \leq \arctan \left(\frac{d_0}{2z_2} \right), \quad (21)$$

This relationship, when combined with equation (17), describes the numerical aperture and resolution limit imposed by the spatial coherence of the imaging system. One should also emphasize that there is another potential limit on the effective numerical aperture of a lensless holographic imaging

system that is imposed by the physical size or the width of the image sensor chip. However, since the on-chip imaging geometry that is depicted in figure 3 has a very small z_2 distance, typically on the order of a few hundred microns or even smaller for higher resolution implementations, using a standard CMOS or CCD based image sensor-array, this physical size of the chip can only be a limiting factor for high-resolution reconstructions where the effective NA approaches the refractive index of the medium, n , which dictates the ultimate diffraction limited NA under vertical illumination. As one example of the level of partial coherence necessary for resolution equivalent to that of a 0.5 NA imaging system, using 500 nm light in air, a light source with bandwidth $\Delta\lambda < 7$ nm positioned at least 2 cm from the sample is sufficient, assuming $D = 100 \mu\text{m}$ and $z_2 = 100 \mu\text{m}$. Such properties can be easily obtained, e.g. using LEDs, modest bandpass filters, and large-core multimode optical fibers.

3.2. Holographic image reconstruction

Provided that the imaging system has a sufficient level of coherence, an in-line hologram will be captured at the image sensor. This hologram is the interference between light that passes directly through the transparent sample, and light that is scattered from objects on the sample plane. Conceptualizing the interference pattern as an in-line hologram, i.e. the interference between an object wave and a reference wave, makes it relatively simple to computationally reconstruct images of the sample based on the intensity directly measured at the image sensor, as will be detailed below.

To begin, we denote the spatially-varying complex amplitude of the time-varying electric field of the light as $E(x, y, z)$. When the light has passed through the sample plane ($z = z_s$), it can be represented as the sum of the incident (reference) light and the scattered (object) light. Assuming the incident wave is a plane wave, we can, without loss of generality, also assume that its phase at the sample plane is zero. The electric field of the light, immediately after passing through the sample plane, can then be written as,

$$\begin{aligned} E(x, y, z_s) &= E_R(x, y, z_s) + E_O(x, y, z_s) \\ &= B_R + B_O(x, y)e^{i\phi_O(x, y)}, \end{aligned} \quad (22)$$

where $B_O(x, y)$ is the amplitude of the object, similar to what one might observe in traditional brightfield transmission microscopy, and $\phi_O(x, y)$ is the phase of the object plane. The general goal of the following analysis is to recover, or reconstruct, the functions B_O and ϕ_O based on holographic measurements.

The propagation of light is in general governed by the Helmholtz differential equation [44],

$$(\nabla^2 + k^2) E(x, y, z) = 0, \quad (23)$$

where $k = 2\pi n/\lambda$. There exist several methods to compute solutions to this equation, including Rayleigh–Sommerfeld diffraction integrals, Fresnel–Kirchhoff diffraction integrals, and the Fresnel and Fraunhofer approximations to these integrals. Here, we will instead use the angular spectrum approach, following Harvey [114] and Goodman [44]. The

angular spectrum approach treats the electric field as a scalar, but other than that makes no approximations regarding the distance of propagation, and is therefore highly accurate, even over very small propagation distances. First, we note that at any given plane (value of z), we can perform a Fourier decomposition to represent the electric field as a sum of plane waves with varying amplitudes travelling in different directions:

$$E(x, y, z) = \iint_{-\infty}^{\infty} A(f_x, f_y, z) e^{i2\pi(f_x x + f_y y)} df_x df_y. \quad (24)$$

Here, $A(f_x, f_y, z)$ is referred to as the angular spectrum of the light. In other words, the electric field is the 2D inverse Fourier transform of its angular spectrum. As the Helmholtz equation is linear (23), one way to ensure that E satisfies it is to require each plane wave component to individually satisfy the Helmholtz equation. Substituting equation (24) into (23) results in,

$$\left[\frac{\partial^2}{\partial z^2} A(f_x, f_y, z) \right] + [-(2\pi f_x)^2 - (2\pi f_y)^2 + k^2] A(f_x, f_y, z) = 0. \quad (25)$$

It can be easily verified via substitution that a general solution of this differential equation is,

$$A(f_x, f_y, z) = A(f_x, f_y, 0) e^{i2\pi f_z(f_x, f_y)z}, \quad (26)$$

$$f_z(f_x, f_y) \equiv \sqrt{\frac{n^2}{\lambda^2} - f_x^2 - f_y^2}, \quad (27)$$

where we have neglected those solutions travelling in the backward (negative z) direction. Note that in terms of wave-propagation, we adopt the notation where e^{ikz} defines the phase accumulation of forward propagation.

As the electric field is the inverse Fourier transform of its angular spectrum, the electric field after propagation can be computed by inverse Fourier transforming equation (26):

$$E(x, y, z) = \mathcal{F}^{-1} \{ \mathcal{F} \{ E(x, y, 0) \} e^{i2\pi f_z z} \} \equiv \mathcal{P}_z \{ E(x, y, 0) \}, \quad (28)$$

where we have used the fact that $A(f_x, f_y, 0)$ is the Fourier transform of the electric field at $z = 0$, and we have also introduced the operator \mathcal{P}_z to represent the forward propagation of light over a distance z . Note that this propagation operator correctly handles those propagating modes corresponding to real f_z as well as evanescent modes that correspond to imaginary f_z , i.e. when $(f_x^2 + f_y^2 > n^2/\lambda^2)$. Such evanescent modes will decay exponentially as the field propagates.

If we apply equation (28) to the light leaving the sample (equation (22)), we find that at the image sensor plane ($z = z_i$),

$$\begin{aligned} E(x, y, z_i) &= \mathcal{P}_{z_2} \{ E(x, y, z_s) \} = B_R e^{ikz_2} + \mathcal{P}_{z_2} \{ E_O(x, y, z_s) \} \\ &= E_R(x, y, z_i) + E_O(x, y, z_i), \end{aligned} \quad (29)$$

where $z_2 = z_i - z_s$ is the distance from the sample to the image sensor. On the right hand side of (29), the first term represents the propagation of the reference plane wave, and the second term represents the scattered object wave. The image sensor is only physically capable of measuring the intensity of this electric field, given by

$$\begin{aligned}
I(x, y, z_i) &= |E(x, y, z_i)|^2 \\
&= |E_R(x, y, z_i)|^2 + E_R^*(x, y, z_i)E_O(x, y, z_i) \\
&\quad + E_R(x, y, z_i)E_O^*(x, y, z_i) + |E_O(x, y, z_i)|^2 \\
&= B_R^2 + B_R e^{-ikz_2} \mathcal{P}_{z_2}\{E_O(x, y, z_s)\} \\
&\quad + B_R e^{ikz_2} (\mathcal{P}_{z_2}\{E_O(x, y, z_s)\})^* + |\mathcal{P}_{z_2}\{E_O(x, y, z_s)\}|^2,
\end{aligned} \tag{33}$$

where $*$ represents complex conjugate. If we assume that the scattered wave intensity is weak compared to the reference wave (typically true for sparse or thin and weakly scattering biological objects), then the last term in equation (30) can be considered negligible compared to the other three terms. With this assumption, it will be possible to reconstruct an ‘image’ of the object by back-propagating the measured intensity through a distance of z_2 . Note that this back-propagation is the inverse of forward propagation because light is time-reversible, i.e. $\mathcal{P}_{-z}\{\mathcal{P}_z\{E\}\} = E$. Back-propagating the captured inline hologram (equation (30)) results in,

$$\begin{aligned}
E_r(x, y, z_s) &= \mathcal{P}_{-z_2}\{I(x, y, z_i)\} \\
&= B_R^2 e^{-ikz_2} + B_R e^{-ikz_2} E_O(x, y, z_s) \\
&\quad + B_R e^{ikz_2} \mathcal{P}_{-z_2}\{(\mathcal{P}_{z_2}\{E_O(x, y, z_s)\})^*\}.
\end{aligned} \tag{31}$$

This reconstructed field consists of a superposition of three terms: a spatially-uniform complex constant, a complex constant times the electric field of the object (what we are trying to recover), and a twin-image term. This twin image term can be thought of as the diffraction pattern resulting from a duplicate, or twin, object located a distance z_2 on the opposite side of the sensor, illuminated in the opposite direction because

$$\begin{aligned}
\mathcal{P}_{-z_2}\{(\mathcal{P}_{z_2}\{E_O(x, y, z_s)\})^*\} &= \mathcal{P}_{-2z_2}\{E_O^*(x, y, z_s)\}, \\
f_x^2 + f_y^2 &< \frac{n^2}{\lambda^2}.
\end{aligned} \tag{32}$$

Visually, it is often possible to discriminate the reconstructed image of the object (2nd term in equation (31)) from the twin image artifact, making the holographic approach practical despite the extraneous twin-image artifact that is spatially overlapping with the real image of the object. There are also more advanced approaches capable of digitally eliminating the twin image term, as described in section 3.7.

While we have shown that $E_r(x, y, z_s)$ contains the object image via equation (31), we have not yet discussed how to compute it in practice. Given that the experimental measurement is $I(x, y, z_i)$, reconstruction of an image requires the computation of $\mathcal{P}_{-z_2}\{I(x, y, z_i)\}$ using the definition in equation (28). As the measured intensity data is sampled discretely via the pixels on the sensor, the reconstruction becomes computationally simple as it is a fast fourier transform (FFT) of the captured hologram multiplied by a known transfer function ($e^{i2\pi f_z z}$), followed by an inverse FFT. Instead of using the kernel $e^{i2\pi f_z z}$ in equation (28), we ignore the evanescent waves as their amplitude will experience a significant decay at the sensor plane and instead use the piecewise function,

In these operations, the amount of computational memory can be an issue for particularly large images unless the images are split into patches and later stitched together. Computational speed is often rather fast, e.g. under 1 s for a 3000×3000 pixel image computed on a consumer laptop, and can be increased even further through the use of graphical processing units (GPUs) [115], which are adept at quickly computing FFTs.

3.3. Applications of computational on-chip imaging

A major benefit of digital holographic reconstruction is that both the amplitude information $B_O(x_s, y_s)$ and phase information $\phi_O(x_s, y_s)$ are recovered. This capability distinguishes holographic imaging from conventional imaging, which is typically only capable of recovering amplitude (or intensity) information. The phase image is similar to what one might observe in a phase-contrast microscope, where contrast indicates difference in sample thickness and/or refractive index. The amplitude and phase channels of information have been used in the basic lensless holography setup to perform blood cell analysis on a chip [116], analyze sperm motility [115, 117, 118], detect waterborne parasites [119], monitor the division of stem cells [120], and provide visual feedback for optoelectronic tweezers [121].

So far we have been focusing on holographic on-chip imaging; however, it is also important to note that on-chip imaging does not necessarily imply holographic imaging. In many lensfree imaging configurations, simple transmission shadow images may be acquired without the possibility of or the need for reconstruction. This may be because the light source is not sufficiently coherent, as discussed in section 3.1, or it may simply be that high resolution is not required for the specific application. Depending on the temporal and spatial coherence of the imaging system, these shadow images may be either diffuse blurs, or they may exhibit fringe-like structures. For small objects, z_2 becomes the limiting factor and determines the resolution of this shadow imaging approach. Nonetheless, distinct patterns can be observed under this shadow imaging approach for many different types of objects. For example, it has been shown that shadow images are sufficient to discriminate among red blood cells, fibroblasts, mES cells, and hepatocytes, despite these objects being of similar sizes [122, 123]. In addition to discrimination tasks, shadow imaging can be helpful for localizing and counting cells, either on a benchtop, or *in situ*, within an incubator. For example, lensfree shadow imaging has been used to monitor mitosis, cell motility, and cell viability [120, 124, 125]. Structured substrates have also been used in some studies to capture specific types of cells in a regular array [126, 127]. In total, the list of different types of cells that have been imaged with shadow based on-chip imaging is quite extensive, including sperm cells, HeLa cells, MDCK cells, leukocytes, cardiomyocytes, human alveolar

epithelial cells, human mesenchymal stem cells, *Pseudomonas aeruginosa*, *Schizosaccharomyces pombe*, A549 cells, NIH 3T3 cells, HepG2 cells, MCF-7 cells, RWPE1 prostate epithelial cells, and bioluminescent *Escherichia coli* [120, 123–125, 128–139].

Another lensfree *non-holographic* on-chip imaging method is to scan the sample across an array of small apertures that are very close to the sample, but not necessarily particularly close to the image sensor. As long as the scanning is precisely controlled, the resolution becomes primarily determined by the aperture size, and is similar in concept to near-field scanning optical microscopy (NSOM). This approach has been combined with microfluidic channels to create an ‘optofluidic microscope’ that operates based on shadow imaging, yet provides microscopic resolution in the observation of *Giardia lamblia*, *C. elegans*, and other small objects [140–142]. Holographic on-chip implementations of optofluidic microscopy [143] and tomography [144] have also been demonstrated, without the use of an array of apertures, which will be further discussed in section 3.4.

Lensfree fluorescence imaging is also possible and shares some characteristics with shadow imaging in that the detected light is incoherent with the incident light, and therefore holographic reconstruction is not possible. In terms of experimental setup, the only additional required component in fluorescence imaging, compared to shadow imaging, is the presence of a filtering mechanism between the sample and image sensor that blocks the excitation light. In order to improve the signal-to-noise performance of these lensfree fluorescent imaging systems, additional strategies may also be used to reduce leakage of excitation light onto the image sensor, including the selection of light source and sensor such that the sensor is insensitive to this light source [145], integrating optical filters directly into the image sensor [146–148], delivering the excitation through total internal reflection [93, 145, 149, 150], and structuring the illumination field [151].

For the most basic lensfree fluorescence on-chip imaging systems, the resolution is intuitively similar to those of the previously discussed shadow imaging systems, where the diffraction of the emitted light over the distance between the sample and sensor is the limiting factor. This diffraction generates a relatively large point spread function (PSF) at the imager chip, whose characteristic size is approximately the same as the sample-sensor distance [145, 149]. As this distance is often several hundreds of microns, the resolution of these fluorescent imaging systems is relatively poor compared to traditional microscopy approaches such as objective-based epi-fluorescence.

To significantly improve the resolution of these lensless fluorescence imaging systems, a number of techniques have been pursued, including both computational and hardware-based approaches. Computationally, deconvolution of the captured image can be used to provide a moderate enhancement to resolution. Using algorithms such as Lucy–Richardson deconvolution, fluorescent lensfree resolutions as good as 40–50 μm have been demonstrated [149, 152, 153]. For better performance than deconvolution, compressive sampling/sensing based decoding approaches such as those introduced

in section 2.3 have been used to achieve resolutions as fine as $\sim 10 \mu\text{m}$. In addition to these computational efforts at improving resolution, some hardware modifications have also been applied, including the incorporation of high-performance micro-filters directly into the image sensor in order to minimize the z_2 distance [147], the use of tapered face-plates to introduce some magnification into the system and mitigate diffraction [150], the nanostructuring of the substrate (discussed in more detail in section 3.9) [31, 32], and the use of actively-structured imaging in a scanning-type configuration through the Talbot effect [154]. Ultimately, the best resolutions of any of these approaches have been on the order of 1–5 μm [31, 32, 150, 154].

Although the majority of lensfree holographic imaging studies have been performed in transmission, there are some instances where reflective imaging is necessary, for example when the sample and/or the substrate is opaque [155]. The challenge in implementing reflection-mode holographic imaging is that the geometric constraints of positioning the light source, sample, and sensor require a relatively large optical path length between the sample and the sensor. As a result of this, the decoupling between spatial resolution and field-of-view, a characteristic feature of lensfree on-chip microscopy in transmission mode, is no longer valid for lensfree reflection imaging. Despite this, lensfree reflection imaging on a chip has been achieved through the use of a beamsplitter cube to direct incident light to the sample, as well as to direct light reflected from the sample to the image sensor [156, 157].

3.4. Resolution limits in holographic on-chip imaging

Of all of the lensfree on-chip imaging modalities discussed thus far, that with the highest potential resolution is the transmissive holographic lensfree imaging. As was discussed in section 3.1, one of the potential limiting factors in resolution for this modality is the coherence of the light source. Yet, as also shown in section 3.1, it is not difficult to construct an imaging system with sufficient coherence for high resolution imaging, and the use of a laser is not necessary. Thus in many practical cases, for the unit-magnification lensfree on-chip imaging geometry the primary resolution-limiting factor becomes the pixel size of the image sensor. Currently, the smallest pixel sizes that are easily available commercially are all greater than 1 μm . If the sensor pixel size was arbitrarily small, the resolution limiting factor could ultimately be due to diffraction, i.e. the evanescent decay of high spatial frequencies, as discussed in section 3.2.

For the intermediate case, where the pixel size is the limiting factor, a few approaches have been developed to close the gap between the pixel size and diffraction limit in resolution. One highly successful approach has been pixel super-resolution. Pixel super-resolution is a technique that was originally developed for other, more conventional, imaging approaches where the resolution is pixel-limited. In this technique, a sequence of images are acquired of the same object where after each successive image, the object is translated across the sensor by distances equal to a non-integer number of pixels. From this sequence of low-resolution, pixelated images, it is

then possible to synthesize a single high-resolution image of the object. As the resolution of the reconstruction is equal to the resolution of the recorded hologram due to the one-to-one magnification in these lensfree on-chip imaging systems, a high-resolution (i.e. pixel super-resolved) hologram will then yield a high-resolution image of the sample.

The first step in synthesizing a pixel super-resolved hologram is to deduce the relative shifts of the low-resolution images with sub-pixel accuracy. Such computations can in general be performed using ‘optical flow’ techniques [158, 159]. One approach that we have used with success is a two-step method, where the shifts are first coarsely determined by cross-correlating the first image with each other image, and later finely determined through an iterative gradient minimization approach. We will describe these shifts between the first image and k th image through a block-circulant matrix denoted F_k . The pixel super-resolved image can then be computed relatively simply as [160],

$$\hat{z} = \left(\sum_{k=1}^N F_k^T D^T y_k \right) / \left(\sum_{k=1}^N F_k^T D^T D F_k \right), \quad (34)$$

where \hat{z} is the pixel-super-resolved hologram represented as a column vector of pixels, D is the down-sampling (decimation) operator that reduces a high-resolution image to the same resolution as the individual low-resolution images, and the y_k are the individual low-resolution images, represented as column vectors. In equation (34), the numerator is essentially the sum of the raw images after correcting for their relative shifts, while the second term is a normalization factor based on the number of images and desired super-resolution factor. Because of the process behind this high-resolution synthesis, this approach is also referred to as ‘*shift and add*’. It is important to note that other approaches exist to synthesizing super-resolved images, for example iterative gradient-descent optimization routines [158].

Although it is possible to shift the image sensor relative to the sample between successive images, it is typically easier to shift the light source relative to the sample, while keeping the image sensor fixed relative to the sample [161]. This also shifts the hologram in the same way that the sun moving overhead shifts an object’s shadow. In this configuration, the relative shift of the hologram is equal to the light source shift, reduced by a factor that is proportional to z_1/z_2 [161]. This reduction means that large shifts of the light source with loose tolerances can be quite sufficient to produce small, sub-pixel level shifts at the image sensor plane with high tolerances. In addition to this light source shifting approach, other ways of capturing multiple images with respective shifts include utilizing an array of closely spaced light sources that are turned on sequentially [162], using a microfluidic device to flow objects across the field of view of the imaging system, capturing multiple images as they flow [143], or introducing variable phase masks into the system [163]. Recent work has also utilized illumination wavelength scanning over a narrow spectral range (e.g. 10–30 nm) to achieve pixel super-resolution in lensfree on-chip microscopy without the need for any sample, sensor or source shifting [75]. In this technique, the

object transmission function is assumed to remain the same over a narrow spectral range, while the holographic diffraction patterns that are sampled at the image sensor chip exhibit relative shifts as a function of the illumination wavelength. A phasor-based new reconstruction algorithm is demonstrated to achieve pixel super-resolution using wavelength scanning with significantly fewer measurements compared to displacement or physical shift based pixel super-resolution approaches. These approaches to improve image resolution through the acquisition of multiple images have been rather successful. In CMOS based imaging sensors, where lensfree holographic imaging has been implemented with pixel sizes as small as 1.12 μm , half-pitch resolutions as fine as 225 nm have been achieved [164, 165], as shown in figure 4(e). This level of resolution is equivalent to that which may be obtained from objective-based microscopes with 0.8–0.9 NA [164, 166]. In section 3.7, we show that it is possible to achieve even higher resolutions using a lensfree synthetic aperture approach.

Although the ultimate resolution is better with CMOS sensors due to their smaller pixel pitch compared to CCDs, pixel super resolution can perhaps be considered even more successful when used in concert with CCDs. Whereas CMOS image sensors are relatively inexpensive and can be manufactured with small pixel sizes, the smallest pixels on CCD image sensors are typically greater than $\sim 4\text{--}5 \mu\text{m}$. Thus there is a larger gap between the pixel size limited resolution of lensfree on-chip microscopy and diffraction-limited resolution, which provides more opportunities for pixel super-resolution to perform, while simultaneously demanding a higher performance from it. Pixel super-resolution has risen to this challenge, and delivered half-pitch resolutions as fine as $\sim 1 \mu\text{m}$ using a CCD, representing an improvement in linear resolution by more than a factor of 5 [164].

One of the enabling elements in using pixel super resolution to extend the resolution this far is the knowledge of the *pixel function* of the image sensor. The best performance is obtained when the sensitivity of the pixel to incoming light is known for each location on the pixel. This responsivity map as a function of space is known as the pixel function. From the most idealized point of view, the pixel function would be uniform and constant across the whole pixel. In practice though, due to electronics and in some cases microlenses added to the sensor design during fabrication, the active area of the pixel does not cover the entire pixel, and the sensitivity of the active area is non-uniform. If the pixel function is known *a priori*, then it can be included as a parameter in the pixel super-resolution algorithms to improve imaging performance. There are two ways that researchers have determined the pixel function: directly measuring it using a focused scanning light source or an NSOM tip, and deducing it through optimization routines that iteratively search for the maximum resolution by varying the pixel function. While the first method presents the advantage of an independent measurement, the accuracy of this measurement is limited by minimum size achievable via a focused light source, which itself is diffraction limited unless e.g. an NSOM probe is used (assuming that the pixel active area is available for the probe tip to approach, which is often times rather difficult practically). Thus, the first approach is

not well-suited for measuring the pixel function of CMOS sensors where the pixel size is already close to the diffraction-limited spot size. However, for CCD image sensors, this has proven to be a viable approach [164]. For CMOS image sensors, the second approach is preferable, and has been used to achieve competitive spatial resolutions as illustrated in figure 4(e) [164].

Although we have focused here on its application to lens-free holographic imaging, pixel super resolution and similar techniques have also been used in other on-chip imaging applications. One example is a non-holographic lensfree on-chip imaging approach, where the sample to sensor distance is extremely small. In this example resolutions as fine as 0.75 μm have been achieved using pixel super resolution based on microfluidic flow [167, 168]. An approach called ‘ePetri’ has also taken advantage of pixel super resolution, where the shifted images are generated by a shifting overhead light source [169–171].

3.5. Sensing limits in holographic on-chip imaging

A separate, but related, microscopy goal to resolution is that of sensitivity. Here, the challenge is not the ability to discern two closely spaced features, but rather, the ability to detect and localize small objects. Such objects can be challenging to detect because their scattering, or their fluorescence emission, may be so small that it becomes buried in background noise related to, e.g. nonuniform illumination, imperfect sensors, shot noise, autofluorescence, or filter leakage. The central issue is the signal to noise ratio (SNR) of the detection platform, which may be enhanced either by increasing the signal from the target objects, or by reducing the noise of the detection system or a combination of both. Sensitivity and resolution are related in one sense because often, high resolution imaging systems yield greater signals for small objects because the objects’ signals are not blurred by large PSFs. In another sense, high sensitivity can enable high resolution through the ability to better localize small particles with enhanced accuracy in approaches such as photoactivated localization microscopy [17], or stochastic optical reconstruction microscopy [18]. A similar argument that ties resolution and SNR can also be made for super resolution through frequency extrapolation.

In this subsection, we highlight recent approaches to boost the signals received from small objects imaged using lens-free holographic microscopy. Holographic imaging by itself (through its heterodyne detection) provides a signal advantage when compared to intensity-based imaging approaches such as dark field microscopy. This is because the relevant signal in holography (second term in equation (31)) is proportional to the electric field of the light scattered by the object rather than its intensity. For particles significantly smaller than the wavelength of light being used, their scattered intensity is governed by Rayleigh scattering [172]:

$$I = I_0 \frac{1 + \cos^2 \theta}{2 |\vec{r}|^2} \left(\frac{2\pi}{\lambda} \right)^4 \left(\frac{n^2 - 1}{n^2 + 2} \right)^2 R^6, \quad (35)$$

where I_0 is the incident light intensity, θ is the angle between the incident direction and observer relative to the scatterer, $|\vec{r}|$ is the distance from the scatterer to point of observation, n is the refractive index of the scattering particle, and R is the radius of the particle. This equation assumes that the background medium has a refractive index of 1. Measurement of scattered intensity thus scales with particle size to the sixth power, whereas measurement of holographic signal only scales with particle size to the third power, thus providing a stronger signal for the detection of these small particles. Other interferometric approaches have also taken advantage of this reduction in scaling factor, one notable example being interferometric reflectance imaging [155, 173–175]

Despite this benefit of holographic imaging, typical lens-free on-chip imaging setups have not been able to discriminate particles smaller than ~ 250 nm relative to background noise, when imaged as dry particles adsorbed to a glass coverslip. To significantly reduce the size limit of detectable particles below 250 nm, we have recently developed a family of approaches to self-assemble liquid nanolenses around the target particles. The self-assembly of nanostructures has generated a number of viable approaches to nano-imaging in general [176]. In particular, the liquid nanolenses formed here provide enhanced scattering in the direction of the image sensor. As shown below, this enhanced scattering is sufficient to enable the detection of particles as small as 40 nm.

One way to self-assemble nanolenses around target particles is via a tilting-based approach [177, 178]. Here, the particles of interest are suspended in a liquid mixture of Tris-HCl buffer and polyethylene glycol (PEG). Out of this mixture, the key component is the PEG. PEG is a water-soluble non-toxic polymer. At the molecular weight used here (600 Da), PEG is a liquid in ambient conditions with very low vapor pressure, and thus does not readily evaporate. After the particles are suspended in the liquid, a drop of the suspension is placed on a recently plasma-treated coverglass. The plasma treatment increases the surface energy of the glass, making it strongly hydrophilic with contact angle less than 10° . After letting the droplet rest on the cover glass for between one and five minutes, the glass is gently tilted to the side so that the droplet slowly flows to the edge of the glass. In the wake of this flowing droplet, adsorbed particles remain adhered to the glass and trap droplets of liquid around them, whose characteristic size ranges from the nanoscale to the microscale. These droplets constitute the self-assembled liquid nanolenses, as shown in figure 5(a). When the substrate is subsequently imaged in a lensfree holographic on-chip imaging system, individual particles as small as 100 nm are observable [165, 178]. This covers a size range that includes many viruses, and enabled the detection of adenoviruses and H1N1 influenza viruses [178], as shown in figures 5(b)–(d).

Another method for forming nanolenses based on evaporation of a droplet [179] has shown similar results in terms of minimum detectable particle size of ~ 100 nm [180]. Here the particles of interest are again suspended in aqueous PEG with molecular weight 600 Da, although with an added surfactant, which may either be Tween 20 or Pluronic F68. However, instead of tilting the substrate to let the droplet flow sideways,

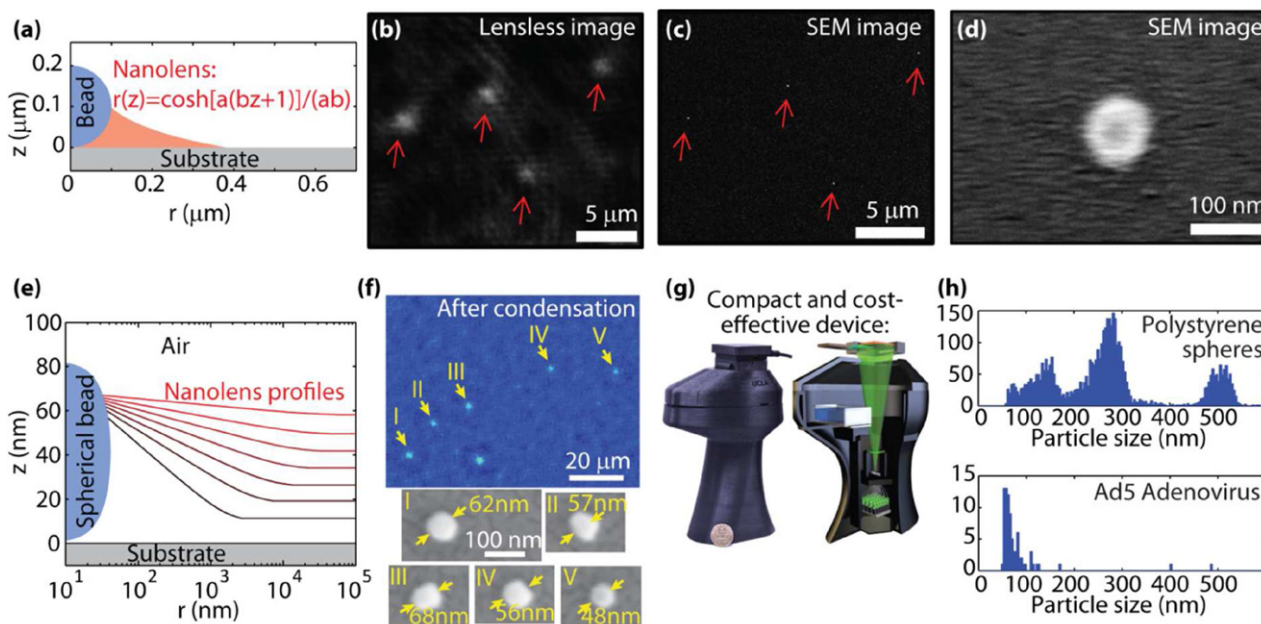


Figure 5. Nanolens formation for lensfree imaging of nanoparticles. (a) A minimal surface, isolated nanolens, as would be formed via a tilting-based procedure. The liquid region is shown in pink, and the equation for the shape of the liquid-air interface is noted in red. (b) A lensfree holographic phase image of individual adenovirus virions, where the necessary level of sensitivity was achieved via isolated nanolenses such as shown in (a). (c) SEM image corresponding to the same region as (b) to verify the location, size, and morphology of the virions. (d) A higher-magnification SEM image of a single adenovirus virion. (e) Continuous film nanolens profiles, such as may be generated from a condensing vapor. (f) A lensfree holographic phase image of several nanoparticles, where the necessary level of sensitivity was achieved via vapor-condensed nanolenses. The lower images show SEM comparisons with accurate sizes. (g) A compact and cost-effective portable device that is capable of both forming vapor-condensed nanolenses as well as imaging them. A photograph and computer-aided design drawing are shown. (h) Particle size histograms of two samples, as imaged with the device shown in (g). Panels (a)–(d) are reproduced from [178], copyright 2013 Nature Publishing Group. Panels (e), (g) and (h) are reproduced from [182], copyright 2015 ACS. Panel (f) is reproduced from [181], copyright 2014 ACS.

the suspension is left for the solvent to evaporate. A film of surfactant and PEG are left behind with embedded particles. This approach has the advantage that no particles are lost from the initial droplet, although it did not demonstrate any improved ability to detect smaller particles. In addition to being used in lensfree holographic imaging, this approach has also been used in combination with conventional low-magnification, low-NA brightfield microscopy to enable the detection of nanoparticles across a wide field of view.

A third method based on the condensation of PEG from the vapor phase has also been employed, which has been able to detect smaller particles, with sizes smaller than 40 nm [181, 182]. This approach also utilizes a plasma-treated cover glass as a substrate. However, the particle deposition can be performed in a variety of different ways, ranging from passive adsorption from a liquid or gas phase suspension to specific capture based on targeted biochemical interactions [181]. Once the particles are captured, the substrate is then dried. At this point, the substrate is exposed for a few minutes to a PEG vapor coming from a modestly heated pool of liquid PEG (~100 °C). In these experiments, a molecular weight of 300Da was used. This PEG vapor then condenses as a thin liquid film on the substrate. Due to surface tension, this film rises in the form of a meniscus in the vicinity of the embedded particles (figure 5(e)), and thus is optically similar to the isolated nanolenses that were left behind in the wake of the receding droplet method. The sample may then be imaged on

a lensfree holographic optical microscope [181] (figure 5(f)), or the imaging may be carried out *in situ* with respect to the film deposition using a field-portable and cost-effective device such as that shown in figure 5(g) [182].

In addition to the ability to detect smaller sized particles, this approach provides the advantage of time-resolved imaging of the nanolens formation [182]. This allowed us to better understand the physics of the process, as well as to ensure that the optimal amount of PEG condensed on the substrate. It was found that the lensfree holographic signal strength at the optimum amount of PEG correlated strongly with the particle size. This approach was used to develop a calibrated measurement tool for particle sizes, with some results presented in figure 5(h). At the low end, this tool could size particles as small as 40 nm, while at the high end, particles potentially up to millimeter scale could be sized. Due to the large field of view, more than 10^5 nanoparticles could be imaged and sized simultaneously. For particles in the range 40–500 nm, the sizing accuracy of individual particles was ± 11 nm. Such sizing capabilities could be compared to existing techniques such as dynamic light scattering [183] or nanoparticle tracking analysis [184].

This condensation of a PEG film has also found applications at the microscale, for conventional fluorescence imaging [185]. Here it was found that a thin liquid film around fluorescent beads with sizes between $2 \mu\text{m}$ and $10 \mu\text{m}$ could significantly enhance the captured fluorescence signal in a conventional fluorescence microscope. In these experiments,

the thin liquid film acted as a reflector, instead of a lens, that helped to redirect fluorescence emission to within the capture angle based on the NA of the microscope objective. This technique could be especially helpful in imaging devices that have a wide field of view, but low NA and therefore comparatively low sensitivity.

3.6. 3D volume imaging and motion tracking

One of the inherent advantages of holographic imaging is its ability to computationally generate focused images at an arbitrary plane after capturing the light. In addition to simplifying the image acquisition procedure at the time of capture, this approach can be used to image objects located at widely varying distances from the image sensor in the same sample, in essence 3D volume imaging. In this context, computational refocusing constitutes the simplest method of volume imaging, where multiple planes are reconstructed via backprojecting a single (possibly pixel-super-resolved, see section 3.4) hologram. For this type of 3D imaging, the resolution in the x and y directions face the same limitations as discussed in section 3.4, however, the z resolution tends to be considerably lower than the x and y resolutions, and for applications such as cell cytometry, axial resolutions of $40\ \mu\text{m}$ or more are typical [186–188].

One way in which the axial localization accuracy of an object can be improved to $\sim 300\text{--}400\text{ nm}$ is through the use of two light sources, where one light source provides normal illumination, and one light source provides oblique illumination [189]. Thus each object in the sample will generate two holograms: one directly beneath the object, and one that is laterally shifted from the object. Using triangulation to find the location where these two reconstructions ‘intersect’ can then provide much greater z localization for a target micro object.

An application where this approach has been applied, and where 3D volume imaging is especially useful, is that of tracking moving micro objects and micro-swimmers, for example live sperm [115, 118]. In these studies, two separate colors are used for the two light sources (i.e. vertical and oblique) to aid in making it unambiguous which hologram was generated from which light source. In this way, thousands of sperm can be tracked simultaneously in a single experiment, in three dimensions, covering a volume of $\sim 5.0\text{ mm} \times 3.5\text{ mm} \times 0.5\text{ mm}$. By tracking this many sperm, it was possible to elucidate rare swimming patterns. For example, in human sperm fewer than 5% followed a helical trajectory, and of those that followed helical trajectories, $\sim 90\%$ were right-handed [115]. Interestingly for horse sperm, left-handed helices were preferred over right-handed ones [118]. The biological reasons for these results are still unknown.

The concept of imaging from multiple angles can be further extended beyond just two angles to a multitude of angles. This approach is in essence a tomography approach, and reconstruction algorithms based on filtered back-projection combined with holographic reconstruction can be used to render 3D images of small micro-objects [186, 190]. In particular, lensfree tomographic microscopy has been used to image *C. elegans* and 3D distributions of beads within a polymer matrix, and has been combined with microfluidic devices

[144, 186, 191]. In these approaches, half-pitch lateral resolutions of $\sim 350\text{ nm}$ and axial resolutions of $\sim 2\ \mu\text{m}$ were obtained over an imaging volume of $\sim 5\text{ mm}^3$ [191].

3.7. Dense sample imaging

One of the key assumptions in holography is that the self-scattering can be considered small in comparison to the interference between scattered light and the reference wave (see equation (30)). In other words, the sample being imaged via an in-line hologram must not be so dense such that there is no clear reference wave. In such situations, one of the basic premises of holographic imaging fails and it is not possible to generate good reconstructions.

However, it is possible to generate excellent reconstructions of such samples using phase recovery techniques instead of holographic reconstruction techniques. In general, phase recovery techniques [55] can be used in coherent imaging systems to deduce the phase of the optical field either from multiple measurements of its intensity (amplitude) or from prior information about the nature of the sample. Once the amplitude and phase of the optical field are known at any plane, the optical field can be reconstructed at any other plane using formulae such as the angular spectrum approach (equation (28)), or the transport of intensity equation [192, 193]. One of the earliest and most famous phase recovery algorithms is the Gerchberg–Saxton algorithm [194], which describes how to determine the phase of an optical field from intensity measurements at two separated planes, for instance plane 1 and plane 2. Roughly, the phase recovery approach is as follows. At plane 1, the intensity is measured, which is proportional to the square of the amplitude. A guess for the phase at this plane is made (often this guess is that $\phi = 0$ everywhere). This complex field consisting of the measured amplitude and guessed phase is then computationally propagated to plane 2 using, e.g. equation (28). At this plane, the amplitude of the computed field is replaced by the experimental measurement, while the computed phase is left untouched. This new complex field is then computationally propagated back to plane 1, the phase is left untouched, and the amplitude is again replaced by the experimental measurement at plane 1. This process can be repeated for many iterations (e.g. until the difference between successive iterations drops below a certain threshold), and eventually the computed amplitude and phase will converge to the real amplitude and phase of the optical field.

These types of phase recovery approaches can be applied to lensfree on-chip imaging as well. One implementation that works with samples that are still somewhat sparse is to assume a uniform intensity and phase of light in regions outside of well-defined objects on the sample [195]. With this assumption, the iterative phase recovery proceeds between two planes, similar to that described above. At the image sensor plane, the optical field amplitude is the known information. At the object, or reconstruction plane, an initial guess for the amplitude and phase of the light is made using the holographic approach discussed in section 3.2. From this guess, ‘background’ regions of the sample (also known as the object support) are defined, and the optical field within these regions

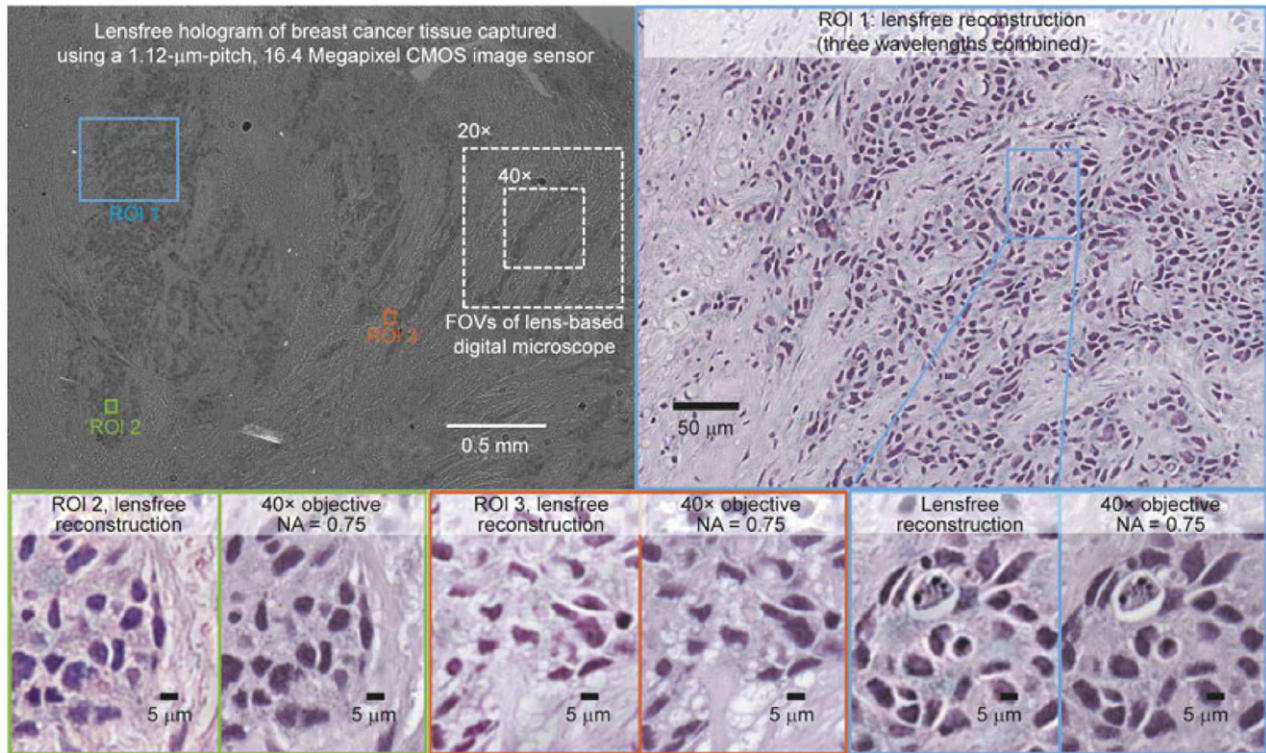


Figure 6. Lensfree imaging via synthetic aperture of a stained human tissue slice. This figure compares lensfree reconstructions using a synthetic aperture phase recovery approach to conventional microscope images. At the level of fine detail, the two modalities compare favorably, however the lensfree imaging modality provides a much greater field of view than either 20× or 40× microscope objectives. Image reproduced from [56], copyright 2015 Nature Publishing Group.

is set to uniform amplitude and phase on each iteration of light propagation. Images acquired using lens-based microscopy can also aid in defining these background regions [157]. These approaches work well to enhance the images acquired from moderately dense samples and to mitigate the effect of the twin image noise.

Another lensfree phase recovery approach is to capture multiple images with variable distances between the sample and image sensor (z_2), while leaving the sample-light source distance (z_1) fixed. With two planes, this technique could directly use the Gerchberg–Saxton algorithm to create a reconstruction. With measurements at more than two planes, the overall reconstruction approach becomes more robust to noise and artifacts, and has enabled the reconstruction of dense samples, such as Papanicolaou smears, dense blood smears, tissue slices, and blood vessel formation [196–199]. Multi-height lensfree microscopy can become even more effective when computationally accounting for slight variations or errors in parallelism between the sample and sensor planes that might be prone to occur when mechanically translating the image sensor, especially in setups that are cost-effective and designed for field use [198].

A third lensfree on-chip phase recovery approach was developed that shares some of the same concepts as synthetic aperture imaging and Fourier ptychographic microscopy (see section 2.2) [56]. In this approach, multiple lensfree on-chip images of the same sample are captured, but from different angles of incidence. These multiple images are then iteratively stitched together in frequency space to form a wide

field-of-view image, with especially high resolution equivalent to 1.4 NA microscope objectives. Redundancy or overlap of the images in the frequency domain is used to perform phase recovery. The field of view of these images is still the full active area of the image sensor, and thus the space-bandwidth product is especially high, on the order of 10^8 – 10^9 . One example is shown in figure 6.

3.8. Color imaging

In holographic imaging, in general, the light source is required to be coherent or partially coherent. One of the implications of this is that the light source is monochromatic or quasi-monochromatic with typical bandwidths less than ~ 3 – 10 nm. As a result, these techniques do not inherently provide color images, although color imaging methods do exist and were used, for example, in the acquisition of the image shown in figure 6. The most straightforward way to acquire color images is to use three different light sources (e.g. red, green, and blue), and acquire images sequentially from each light source. The reconstructions from images can then be used to form the RGB color channels of a color image. Although this procedure is relatively easy, the twin image noise or other reconstruction artifacts from these color channels can lead to rainbow-like artifacts in the resulting images, such as those in figure 7(a) [200–203].

An alternative approach that minimizes such rainbow artifacts is to combine the images in YUV color space instead of RGB color space [200, 201]. In YUV color space, the Y

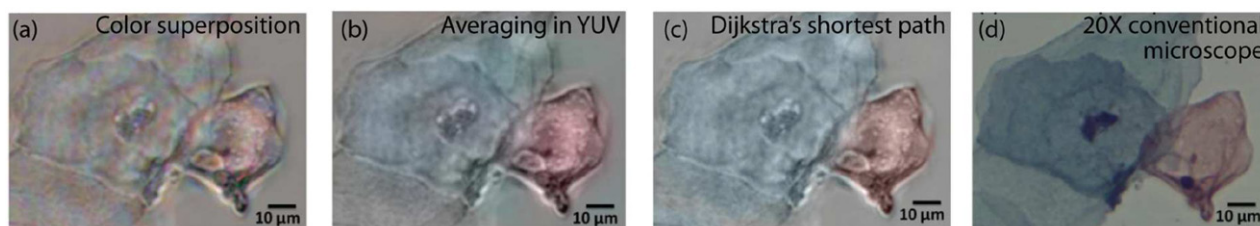


Figure 7. Lensfree color imaging. (a) A simple superposition of reconstructions from three differently colored light sources. Note the rainbow-like artifacts. (b) Superposition of reconstructions from three differently colored light sources, after first converting to YUV color space. Note that the rainbow artifacts have been mitigated. (c) A colorized reconstruction based on Dijkstra's shortest path algorithm. The boundaries for the colorization are acquired from a monochrome reconstruction, while the colors for regions within the boundaries are acquired from spatial averages of the RGB images. (d) A comparison of the same two cells using a conventional brightfield microscope. Figure reproduced from [200], copyright 2013 OSA.

channel contains brightness information, while the U and V channels contain color information. With this method, the pixel super-resolved lensfree reconstruction of the object at the green color is used as the Y channel, whereas a low resolution lensfree RGB image of the object is used to create UV channels, which are then merged with the super-resolved Y channel in YUV color space, and finally converted back to RGB color space for visualization. As can be seen in figure 7(b), this approach is successful in mitigating the rainbow-like color artifacts, while still preserving the resolution and the colors of the sample.

Another technique is based on Dijkstra's shortest path algorithm to colorize a monochromatic reconstruction [200, 204]. Here, the reconstruction from a single color channel is first generated at high resolution through pixel super-resolution. This reconstruction serves to provide sharp, well-defined borders between regions of the sample. The other color channels are then holographically reconstructed at comparably lower resolution. Colors for different regions within the image are determined by averaging all of the color information around a small neighborhood within a region. This neighborhood should be large enough that it would span several fringes of the rainbow-like artifacts, but not so large that it encompasses many different regions of the sample that would have different colors. The color for each region is then spread, or 'filled' throughout the reconstruction until it hits a border defined by the high-resolution monochrome image. The algorithmic approach here is similar to that used in watershed algorithms. As can be seen in figure 7(c), the Dijkstra approach is successful at colorizing samples, without rainbow artifacts. However this approach could fail where a single object gradually changes in hue across the field of view.

In many biomedical applications, such as tissue staining, the primary purpose of the stain is to provide brightness contrast and not to impart multiple colors onto the sample. However, pathologists are familiar with and trained at making diagnoses based on the colored image, and it is therefore advantageous to be able to generate colored images for their use. In such cases where color is desirable, but different hues are unnecessary, a single monochrome image acquired using a single wavelength can be colorized using an intensity-to-color mapping function. While it does not add any new information to the image, it does present the image in a format more familiar for pathologists. This statistical approach has been

used in the reconstruction of breast cancer tissue slices, for example [198].

In addition to helping make images more valuable qualitatively, quantitative measurements of color have been used to discriminate between different types of objects on a sample. One example is the discrimination of CD4 and CD8 cells using plasmonic labels [205]. The relative populations of CD4 and CD8 cells indicate the progression of HIV as well as efficacy of treatment. Unfortunately, these two types of cells look virtually identical under conventional microscopy approaches. To distinguish them using lensfree holographic microscopy, plasmonic labels were used, where silver nanoparticles were functionalized with antibodies to specifically bind to CD8 cells, while gold nanoparticles were functionalized to specifically bind to CD4 cells. Because the plasmon resonances of silver and gold result in significantly different colors of scattered light, multi-color lensfree imaging made it possible to distinguish these two types of cells with high accuracy, when combined with a machine learning algorithm.

3.9. Integrating nanostructured substrates for lensfree sensing

In addition to direct microscopic imaging of samples, lensfree platforms can also be used to sense small particles or biomolecules. Section 3.5 discussed ways to sense individual particles as small as ~ 40 nm. However, there is a need to sense many kinds of even smaller particles as well molecules [206–208]. Although lensfree imaging is not yet capable of sensing *individual* particles smaller than ~ 40 nm, it has been shown to be able to sense concentrations and films of such particles. To accomplish this, lensfree microscopy has been combined with specially-structured substrates to promote sensitivity to biomolecules. These types of structures include both regularly-structured as well as randomly-structured substrates.

One type of regularly structured substrate, a plasmonic nanohole array, has been shown to exhibit extraordinary optical transmission at specific resonant wavelengths [209]. These resonances are particularly sensitive to the refractive index of the material in the evanescent region of the metal-dielectric interfaces [210]. As such, sensing mechanisms based on these devices are good candidates for the sensing of small objects or thin films of biomolecules that can be specifically bound to the surface using e.g. an antibody-antigen interaction. When

the target molecule binds, it displaces some water, increasing the local refractive index, which provides the opportunity for a detection event. This principle has been combined with microfluidic devices and field-portable lensfree imaging systems to sense refractive index changes of $\sim 2 \times 10^{-3}$ in fluids using an array of slits [211]. It has also been combined with an array of plasmonic holes for sensing monolayers of bound proteins with similar sensitivity in terms of refractive index units [212]. Differential measurements using two light sources at different wavelengths have also been used to improve the signal to noise performance of this lensfree plasmonic sensing system on a chip [213].

Aperiodic and randomly-nanostructured substrates have also proven useful in improving imaging performance in incoherent, fluorescent lensfree imaging platforms, which were briefly discussed in section 3.3. In these incoherent imaging modalities, holography is not feasible, and therefore the images captured using lensless imaging systems tend to be rather low resolution. One solution to boost resolution used a nanostructured substrate placed in close proximity to the point emitters or scatterers [32]. This nanostructured substrate encoded the diffracted field with a point-spread function whose far-field shape was very sensitively dependent on the location of origin. Through precise calibration, it was possible to invert the scattering problem to understand the distribution of emitter locations with high resolution. Depending on the nature of the sample and imaging system, compressive sampling/sensing based decoding approaches such as those discussed in section 2.3 were also applied [31].

The substrate being imaged can also be structured *in situ* through the binding of particles that act as labels; when a particle binds, it indicates the sensing of a target agent. The sensing can be accomplished through a sandwich assay for a small biomolecule, where if that molecule is present, it will bind to the substrate, and then tether a bead functionalized for it. The bead is then detected using a lensfree imaging system because the biomolecule itself would have been too small to detect on a chip [214, 215].

4. Compact and field-portable microscopy platforms

One of the important advantages of many of the microscopy techniques described in sections 2 and 3 is their experimental robustness. In comparison to standard laboratory microscopy modalities, computational microscopy approaches are capable of providing very high quality images even when implemented in platforms that are small, cost-effective, and field-portable. This is particularly true for the lensfree on-chip imaging platforms, which obviate the need for objective lenses and long object-to-sensor path lengths [216]. Such platforms can have applications in point-of-care diagnostic devices for use in the field, or in global health settings where resources may be limited and rapid diagnostics in demand [217], as well as scientific and educational applications where cheap accessible devices may help to democratize and expose a larger proportion of the world to scientific inquiry [9, 218].

4.1. Portable lens-based devices

In recent years, the proliferation of small, portable, and relatively inexpensive consumer devices such as smartphones, tablets, and ultrabooks has provided a unique opportunity to develop microscopic imaging platforms that are themselves simultaneously high-performance, compact, and portable. One class of such platforms are those based around the image sensors and camera modules that are present in virtually all smartphones and tablets. With some additional external hardware it is possible to convert these devices into high-performance microscopes. One of the primary modalities pursued with these devices is fluorescent microscopy. The major components required in addition to the consumer imaging device and its camera include a light source, lenses for magnification, a focusing mechanism, and filters to block excitation light but pass emitted light [219]. Figure 8 shows several such devices. The device shown in figures 8(a) and (b) has been used to perform blood analysis on a cell phone [220]. Using various filter attachments, it is capable of counting red blood cells, white blood cells, and hemoglobin density. Similar field-portable devices have also been used to detect hormone levels in cow milk using a bead-based fluorescent assay [221]. With some of the newer, high-performance image sensors found in smartphones, it has been shown to be possible to demonstrate excellent sensitivity to fluorescent objects such as nanoparticles and viruses [222], as well as individual DNA segments, whose length can be accurately measured using the phone itself (figures 8(d) and (e)) [223]. Cell-phone based fluorescent microscopes have also been developed to test water quality and screen for the presence of *G. lamblia* through fluorescent labeling and machine learning (figures 8(f) and (g)) [224]. These results are particularly significant, as it is possible to detect concentrations as low as ~ 12 cysts per 10 ml.

In addition to cell-phone platforms developed exclusively for fluorescence, a number of multi-modality portable microscope platforms have been developed that are capable of bright-field imaging, as well as fluorescence, and sometimes darkfield. Fletcher *et al* have developed a range of microscopes with high-resolution brightfield and fluorescence capabilities based around a cell phone, particularly for global health applications [225, 226]. The most recent of these they refer to as CellScope (figure 8(c)), which they have used in a number of applications, including the detection of tuberculosis bacteria [227–229] and the detection of blood-borne parasites [230, 231]. They have also developed another cell-phone based microscope platform for use in retinal imaging [232, 233].

The development of imaging platforms that can be used ubiquitously is also desirable to simplify the process of interfacing the platforms with existing hardware throughout the world. Attachments compatible with a range of mobile phones present one solution [234]. Another solution is a particularly cost-effective multi-modal microscope that uses very inexpensive ball lenses with focusing and sample placement achieved by the simple folding of paper [230, 235]. By itself, this device can be used for visual inspection, or it may also be connected to an external image capture device.

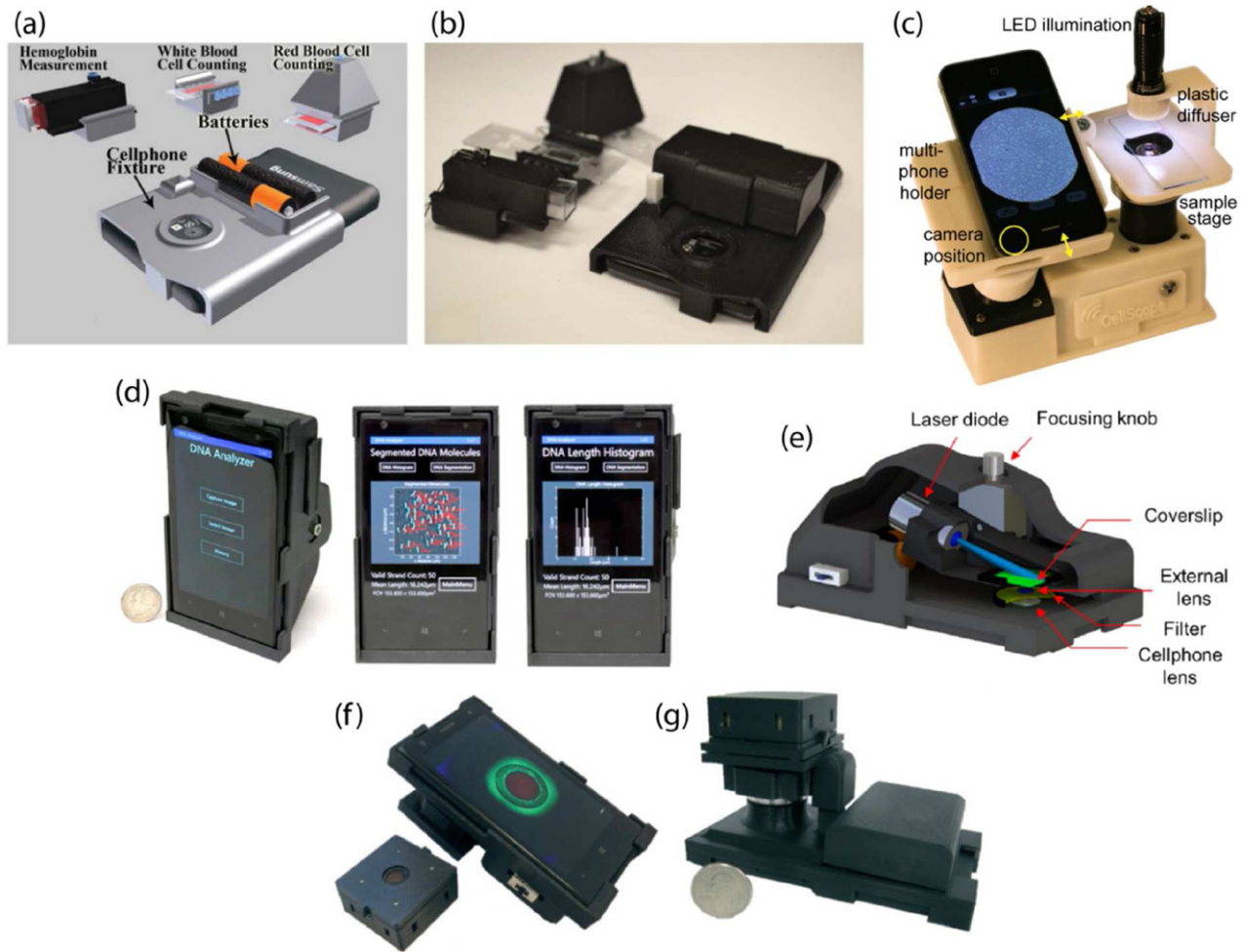


Figure 8. Portable lens-based microscopy platforms. (a) and (b) A family of smart-phone attachments designed to quantify different components in blood. (c) A small portable microscopy platform built around a smartphone. (d) and (e) A smartphone microscopy platform capable of imaging and sizing individual segments of DNA. (f) and (g) A smartphone microscopy platform used to screen water samples for the presence of *G. lamblia* cysts. Panels (a) and (b) reproduced from [220], copyright 2013 RSC. Panel (c) reproduced from [234], copyright 2014 PLOS. Panels (d) and (e) reproduced from [223], copyright 2014 ACS. Panels (f) and (g) reproduced from [224], copyright 2015 RSC.

Some of the computational techniques specifically discussed in sections 2 and 3 have also been implemented in compact and cost-effective platforms. In section 4.2, we present an extended discussion on the applications of such field-portable lensfree holographic imaging devices. Another example is the use of an LED array for illumination control similar to the Fourier ptychographic microscopy discussed in section 2.2. This illumination scheme has been combined with a cell-phone based microscope to enable brightfield, darkfield, and phase images with computational refocusing capability [236].

4.2. Portable lensfree devices

Many of the lensfree microscopy approaches discussed in section 3 have also been implemented in small field-portable systems. In these approaches, no expensive lensing elements are necessary, which helps to further reduce costs compared to devices based on lenses with expensive aberration-correcting designs. The most rudimentary lensless imaging platforms are based on shadow imaging, where no digital reconstruction of the sample is performed, as described in section 3.3. Images

were captured and used as-is, rather than using them as a basis for reconstructing in-focus images of the sample. These shadow imaging approaches are still being used in a number of applications where high resolution is not necessary. Some examples include cell-counting or tracking applications where it is not necessary to see the morphology of cells or their sub-cellular components, but it is enough to know that a cell exists and where it is. Several field-portable implementations of lensfree shadow imaging have been developed, including ones that interface with cell phone image sensors directly [237], or via a fiber-optic faceplate relay [238].

A number of platforms have also been developed where the lensfree imaging system is constructed externally to the cell phone or other computing device. In these cases, captured images are typically transferred using a USB cable, and reconstruction of the images is performed computationally, as discussed in section 3. These devices include ones that do not provide any pixel-super resolution capabilities [195], as well as ones where pixel super-resolution (see section 3.4) is implemented via an array of LEDs connected to optical fibers [162, 201, 217]. Other portable variations of these devices have

also been created that generate nano-lenses for small particle sensing as illustrated in section 3.5 [182], perform the tomographic imaging discussed in section 3.6 [239], perform the multi-height image capture discussed in section 3.7 [197, 201], perform color imaging as discussed in section 3.8 [201], or sense biomolecules using the nanostructured substrates discussed in section 3.9 [212, 213]. Reflection imaging variants have also been constructed [157].

Several portable devices have also been constructed based on other computational imaging concepts. One set of such devices is based on the ePetri platform, where a shifting light source with a relatively large shift range illuminates a sample that is held very close (on the order of $1\ \mu\text{m}$) to the active area of the image sensor. In these field-portable devices, a smartphone display was used to create the scanning light source, and an external image sensor was used to capture the images [169]. These devices have been used inside cell incubators to track the long-term growth and proliferation of cell cultures, as well as to track the motion of more rapidly motile microorganisms such as *Euglena gracilis* [170]. A variety of other lensfree imaging devices have also been used in incubator systems, including shadow imaging systems [240], as well as ones based on the Talbot effect [154]. Finally, portable devices based around the optofluidic microscope with small apertures placed in close proximity to the sample (section 3.3) have also been developed for color imaging of red blood cells potentially infected with malaria parasites [241].

5. Future outlook

Computational microscopy is still a burgeoning field, and there are several avenues and room for improvement. With regard to virtually all techniques mentioned here, it is always desirable to attain higher resolution. Many techniques such as the lensfree imaging via synthetic aperture approach discussed in section 3.7 are currently pushing the limits of diffraction, and so one route for improved resolution could potentially come via combination of the computational imaging techniques discussed here with superresolution microscopy approaches. Incoherent computational imaging techniques can be combined some of the recently-developed superresolution approaches like localization microscopy or stimulated emission-depletion microscopy, while coherent computational imaging techniques can be combined with superresolution approaches such as nonlinear microscopy. There is also the potential for further resolution improvements through purely computational means and the improvement of signal to noise ratios.

In a complimentary fashion to improvements in resolution, we also expect to see concomitant improvements in sensitivity. Although self-assembled nanolenses have been used to detect individual particles as small as $\sim 40\text{nm}$, there are many smaller objects whose sensing/detection is important. Some examples include ribosomes, proteins, RNA fragments, and DNA fragments. The development of higher-performance nanolens approaches could enable the sensing of these smaller particles. In addition, it would simplify processing

and the range of samples that could be analyzed if nanolenses were not necessary to see these smaller particles. Improving the sensitivity of unaided lensfree holographic imaging (i.e. without nanolenses) is also something we expect to see in the near future.

Another area of improvement that would increase the impact of computational microscopy is the improvement in imaging speed such that it is possible to perform real-time imaging. Most of the computational imaging techniques require the acquisition of many raw frames to synthesize a single reconstructed frame. Such techniques included structured illumination microscopy (section 2.2), synthetic aperture microscopy (section 2.2), Fourier ptychographic microscopy (section 2.2), pixel super-resolved lensfree holographic microscopy (section 3.4), and dense sample imaging via iterative phase recovery (section 3.7). The acquisition of many raw frames in each of these techniques can take considerable time, which can limit these techniques' applicability in live-cell imaging, for instance. Finding ways to more quickly acquire the necessary raw data would help to solve this challenge.

Another challenge in high-speed imaging is that of the data processing. Some computational microscopy approaches require considerable computational power, and can thus take significant time to compute reconstructions. In most cases, the time to compute a reconstruction is longer than the time necessary to acquire the raw data. However, many reconstruction algorithms could be programmed in a parallel-computation-friendly manner for implementation using graphical processing units (GPUs), which can dramatically increase the reconstruction speed. Furthermore, the development of more efficient algorithms, such as new phase recovery algorithms could also help to improve reconstruction time.

One last major area of future improvement will be in the use and distribution of compact field-portable microscopy platforms, especially in resource-limited settings. Although many of these approaches have been specifically designed for use in point-of-care or global health applications, their actual testing and adoption in these settings has thus far been limited, although some studies of their performance in these settings have been already performed [230, 242]. More intensive testing in these settings can help to refine the designs and guide improvements to future generations of devices to make sure they meet the real demands in the field.

References

- [1] Hooke R 1665 *Micrographia* (London: The Royal Society)
- [2] Bardell D 2004 The biologists' forum: the invention of the microscope *BIOS* **75** 78–84
- [3] Ahrens M B, Orger M B, Robson D N, Li J M and Keller P J 2013 Whole-brain functional imaging at cellular resolution using light-sheet microscopy *Nat. Methods* **10** 413–20
- [4] Webb R H 1996 Confocal optical microscopy *Rep. Prog. Phys.* **59** 427
- [5] Corle T R and Kino G S 1996 *Confocal Scanning Optical Microscopy and Related Imaging Systems* (New York: Academic)
- [6] Xu C, Zipfel W, Shear J B, Williams R M and Webb W W 1996 Multiphoton fluorescence excitation: new spectral

- windows for biological nonlinear microscopy *Proc. Natl Acad. Sci.* **93** 10763–8
- [7] So P T C, Dong C Y, Masters B R and Berland K M 2000 Two-photon excitation fluorescence microscopy *Annu. Rev. Biomed. Eng.* **2** 399–429
- [8] Helmchen F and Denk W 2005 Deep tissue two-photon microscopy *Nat. Methods* **2** 932–40
- [9] Ozcan A 2014 Mobile phones democratize and cultivate next-generation imaging, diagnostics and measurement tools *Lab Chip* **14** 3187–94
- [10] Vashist S K, Mudanyali O, Schneider E M, Zengerle R and Ozcan A 2013 Cellphone-based devices for bioanalytical sciences *Anal. Bioanal. Chem.* **406** 3263–77
- [11] Hill S A *A Complete History of the Camera Phone* (Digital Trends)
- [12] Ozcan A and McLeod E 2016 Lensless imaging and sensing *Annu. Rev. Biomed. Eng.* **18** 77–102
- [13] Sahl S J and Moerner W 2013 Super-resolution fluorescence imaging with single molecules *Curr. Opin. Struct. Biol.* **23** 778–87
- [14] Nienhaus K and Nienhaus G U 2014 Fluorescent proteins for live-cell imaging with super-resolution *Chem. Soc. Rev.* **43** 1088–106
- [15] Small A and Stahlheber S 2014 Fluorophore localization algorithms for super-resolution microscopy *Nat. Methods* **11** 267–79
- [16] Deschout H, Zancacchi F C, Mlodzianoski M, Diaspro A, Bewersdorf J, Hess S T and Braeckmans K 2014 Precisely and accurately localizing single emitters in fluorescence microscopy *Nat. Methods* **11** 253–66
- [17] Betzig E, Patterson G H, Sougrat R, Lindwasser O W, Olenych S, Bonifacino J S, Davidson M W, Lippincott-Schwartz J and Hess H F 2006 Imaging intracellular fluorescent proteins at nanometer resolution *Science* **313** 1642–5
- [18] Rust M J, Bates M and Zhuang X 2006 Sub-diffraction-limit imaging by stochastic optical reconstruction microscopy (STORM) *Nat. Methods* **3** 793–6
- [19] Lippmann G 1908 Epreuves reversibles donnant la sensation du relief *J. Phys. Theor. Appl.* **7** 821–5
- [20] Levoy M, Zhang Z and Mcduwall I 2009 Recording and controlling the 4D light field in a microscope using microlens arrays *J. Microsc.* **235** 144–62
- [21] Adelson E H and Wang J Y A 1992 Single lens stereo with a plenoptic camera *IEEE Trans. Pattern Anal. Mach. Intell.* **14** 99–106
- [22] Tanida J, Kumagai T, Yamada K, Miyatake S, Ishida K, Morimoto T, Kondou N, Miyazaki D and Ichioka Y 2001 Thin observation module by bound optics (TOMBO): concept and experimental verification *Appl. Opt.* **40** 1806
- [23] Ng R 2005 Fourier slice photography *ACM SIGGRAPH 2005 Papers* (New York: ACM) pp 735–44
- [24] Levoy M, Ng R, Adams A, Footer M and Horowitz M 2006 Light field microscopy *ACM SIGGRAPH 2006 Papers* (New York: ACM) pp 924–34
- [25] Jang J-S and Javidi B 2004 3D integral imaging of micro-objects *Opt. Lett.* **29** 1230
- [26] Kak A C and Slaney M 2001 *Principles of Computerized Tomographic Imaging* (Philadelphia: Society for Industrial and Applied Mathematics)
- [27] Navarro H, Barreiro J C, Saavedra G, Martínez-Corral M and Javidi B 2012 High-resolution far-field integral-imaging camera by double snapshot *Opt. Express* **20** 890
- [28] Llavador A, Sánchez-Ortiga E, Barreiro J C, Saavedra G and Martínez-Corral M 2015 Resolution enhancement in integral microscopy by physical interpolation *Biomed. Opt. Express* **6** 2854
- [29] Broxton M, Grosenick L, Yang S, Cohen N, Andalman A, Deisseroth K and Levoy M 2013 Wave optics theory and 3D deconvolution for the light field microscope *Opt. Express* **21** 25418
- [30] Cohen N, Yang S, Andalman A, Broxton M, Grosenick L, Deisseroth K, Horowitz M and Levoy M 2014 Enhancing the performance of the light field microscope using wavefront coding *Opt. Express* **22** 24817
- [31] Khademhosseini B, Biener G, Sencan I and Ozcan A 2010 Lensfree color imaging on a nanostructured chip using compressive decoding *Appl. Phys. Lett.* **97** 211112
- [32] Khademhosseini B, Sencan I, Biener G, Su T-W, Coskun A F, Tseng D and Ozcan A 2010 Lensfree on-chip imaging using nanostructured surfaces *Appl. Phys. Lett.* **96** 171106
- [33] Wu J, Lin X, Liu Y, Suo J and Dai Q 2014 Coded aperture pair for quantitative phase imaging *Opt. Lett.* **39** 5776
- [34] Kwon K-C, Jeong J-S, Erdenebat M-U, Lim Y-T, Yoo K-H and Kim N 2014 Real-time interactive display for integral imaging microscopy *Appl. Opt.* **53** 4450
- [35] Kwon K-C, Jeong J-S, Erdenebat M-U, Piao Y-L, Yoo K-H and Kim N 2015 Resolution-enhancement for an orthographic-view image display in an integral imaging microscope system *Biomed. Opt. Express* **6** 736
- [36] Wang S, Liu W, Wang A, Li Y and Ming H 2014 An integral imaging method for depth extraction with lens array in an optical tweezer system *Proc. SPIE* **9270** 927000
- [37] Javidi B and Okano F (ed) *3D Television, Video, and Display Technologies* ed B Javidi (Berlin: Springer)
- [38] Kim J, Jung J-H, Jeong Y, Hong K and Lee B 2014 Real-time integral imaging system for light field microscopy *Opt. Express* **22** 10210
- [39] Lin X, Wu J, Zheng G and Dai Q 2015 Camera array based light field microscopy *Biomed. Opt. Express* **6** 3179
- [40] Prevedel R *et al* 2014 Simultaneous whole-animal 3D imaging of neuronal activity using light-field microscopy *Nat. Methods* **11** 727–30
- [41] Sakmann K and Kasevich M 2014 Single-shot 3D imaging of dilute atomic clouds *Opt. Lett.* **39** 5317
- [42] Gustafsson M G L 2000 Surpassing the lateral resolution limit by a factor of two using structured illumination microscopy *J. Microsc.* **198** 82–7
- [43] Frohn J T, Knapp H F and Stemmer A 2000 True optical resolution beyond the Rayleigh limit achieved by standing wave illumination *Proc. Natl Acad. Sci.* **97** 7232–6
- [44] Goodman J 2004 *Introduction to Fourier Optics* (Greenwood Village, CO: Roberts and Company Publishers)
- [45] Hirano Y, Matsuda A and Hiraoka Y 2015 Recent advancements in structured-illumination microscopy toward live-cell imaging *Microscopy* **64** 237–49
- [46] Gustafsson M G L 2005 Nonlinear structured-illumination microscopy: Wide-field fluorescence imaging with theoretically unlimited resolution *Proc. Natl. Acad. Sci. U. S. A.* **102** 13081–6
- [47] Li D *et al* 2015 Extended-resolution structured illumination imaging of endocytic and cytoskeletal dynamics *Science* **349** aab3500
- [48] Zhao M, Zhang H, Li Y, Ashok A, Liang R, Zhou W and Peng L 2014 Cellular imaging of deep organ using two-photon Bessel light-sheet nonlinear structured illumination microscopy *Biomed. Opt. Express* **5** 1296
- [49] Komis G, Mistrik M, Šamajová O, Ovečka M, Bartek J and Šamaj J 2015 Superresolution live imaging of plant cells using structured illumination microscopy *Nat. Protocols* **10** 1248–63
- [50] Turpin T M, Gesell L H, Lapidus J and Price C H 1995 Theory of the synthetic aperture microscope *Proc. SPIE* **2566** 230–40
- [51] Schwarz C J, Kuznetsova Y and Brueck S R J 2003 Imaging interferometric microscopy *Opt. Lett.* **28** 1424
- [52] Ralston T S, Marks D L, Scott Carney P and Boppart S A 2007 Interferometric synthetic aperture microscopy *Nat. Phys.* **3** 129–34

- [53] Indebetouw G, Tada Y, Rosen J and Brooker G 2007 Scanning holographic microscopy with resolution exceeding the Rayleigh limit of the objective by superposition of off-axis holograms *Appl. Opt.* **46** 993
- [54] Kuznetsova Y, Neumann A and Brueck S R 2007 Imaging interferometric microscopy? approaching the linear systems limits of optical resolution *Opt. Express* **15** 6651–63
- [55] Fienup J R 1982 Phase retrieval algorithms: a comparison *Appl. Opt.* **21** 2758
- [56] Luo W, Greenbaum A, Zhang Y and Ozcan A 2015 Synthetic aperture-based on-chip microscopy *Light Sci. Appl.* **4** e261
- [57] Mico V, Zalevsky Z and García J 2007 Synthetic aperture microscopy using off-axis illumination and polarization coding *Opt. Commun.* **276** 209–17
- [58] Gutzler T, Hillman T R, Alexandrov S A and Sampson D D 2010 Coherent aperture-synthesis, wide-field, high-resolution holographic microscopy of biological tissue *Opt. Lett.* **35** 1136
- [59] Kim M, Choi Y, Fang-Yen C, Sung Y, Dasari R R, Feld M S and Choi W 2011 High-speed synthetic aperture microscopy for live cell imaging *Opt. Lett.* **36** 148
- [60] Alexandrov S A, Hillman T R, Gutzler T and Sampson D D 2006 Synthetic aperture fourier holographic optical microscopy *Phys. Rev. Lett.* **97** 168102
- [61] Mico V, Zalevsky Z, García-Martínez P and García J 2006 Synthetic aperture superresolution with multiple off-axis holograms *J. Opt. Soc. Am. A* **23** 3162
- [62] Di J, Zhao J, Jiang H, Zhang P, Fan Q and Sun W 2008 High resolution digital holographic microscopy with a wide field of view based on a synthetic aperture technique and use of linear CCD scanning *Appl. Opt.* **47** 5654
- [63] Hillman T R, Gutzler T, Alexandrov S A and Sampson D D 2009 High-resolution, wide-field object reconstruction with synthetic aperture Fourier holographic optical microscopy *Opt. Express* **17** 7873
- [64] Granero L, Micó V, Zalevsky Z and García J 2010 Synthetic aperture superresolved microscopy in digital lensless fourier holography by time and angular multiplexing of the object information *Appl. Opt.* **49** 845
- [65] Tippie A E, Kumar A and Fienup J R 2011 High-resolution synthetic-aperture digital holography with digital phase and pupil correction *Opt. Express* **19** 12027
- [66] Zheng G, Horstmeyer R and Yang C 2013 Wide-field, high-resolution Fourier ptychographic microscopy *Nat. Photon.* **7** 739–45
- [67] Zhang Y, Jiang W, Tian L, Waller L and Dai Q 2015 Self-learning based Fourier ptychographic microscopy *Opt. Express* **23** 18471
- [68] Tian L, Li X, Ramchandran K and Waller L 2014 Multiplexed coded illumination for fourier Ptychography with an LED array microscope *Biomed. Opt. Express* **5** 2376
- [69] Horstmeyer R, Chen R Y, Ou X, Ames B, Tropp J A and Yang C 2015 Solving ptychography with a convex relaxation *New J. Phys.* **17** 053044
- [70] Li P, Batey D J, Edo T B and Rodenburg J M 2015 Separation of 3D scattering effects in tilt-series fourier ptychography *Ultramicroscopy* **158** 1–7
- [71] Ma C, Liu Z, Tian L, Dai Q and Waller L 2015 Motion deblurring with temporally coded illumination in an LED array microscope *Opt. Lett.* **40** 2281
- [72] Liu Z, Tian L, Liu S and Waller L 2014 Real-time brightfield, darkfield, and phase contrast imaging in a light-emitting diode array microscope *J. Biomed. Opt.* **19** 106002
- [73] Tian L and Waller L 2015 Quantitative differential phase contrast imaging in an LED array microscope *Opt. Express* **23** 11394
- [74] Li Z, Zhang J, Wang X and Liu D 2014 High resolution integral holography using Fourier ptychographic approach *Opt. Express* **22** 31935
- [75] Luo W, Zhang Y, Feizi A, Gorocs Z and Ozcan A 2016 Pixel super-resolution using wavelength scanning *Light Sci. Appl.* **5** e16056
- [76] Candes E J, Romberg J and Tao T 2006 Robust uncertainty principles: exact signal reconstruction from highly incomplete frequency information *IEEE Trans. Inf. Theory* **52** 489–509
- [77] Candes E J and Tao T 2006 Near-optimal signal recovery from random projections: universal encoding strategies? *IEEE Trans. Inf. Theory* **52** 5406–25
- [78] Donoho D L 2006 Compressed sensing *IEEE Trans. Inf. Theory* **52** 1289–306
- [79] Candes E J and Wakin M B 2008 An introduction to compressive sampling *IEEE Signal Process. Mag.* **25** 21–30
- [80] Daubechies I 1992 *Ten Lectures on Wavelets* (Philadelphia, PA: Society for Industrial and Applied Mathematics)
- [81] Mallat S 2008 *A Wavelet Tour of Signal Processing Third Edition: The Sparse Way* (Boston: Academic)
- [82] Vandenberghe L and Boyd S 1996 Semidefinite programming *SIAM Rev.* **38** 49–95
- [83] Romberg J 2008 Imaging via compressive sampling *IEEE Signal Process. Mag.* **25** 14–20
- [84] Takhar D, Laska J N, Wakin M B, Duarte M F, Baron D, Sarvotham S, Kelly K F and Baraniuk R G 2006 A new compressive imaging camera architecture using optical-domain compression *Proc. SPIE* **6065** 606509
- [85] Duarte M F, Davenport M A, Takhar D, Laska J N, Sun T, Kelly K F and Baraniuk R G 2008 Single-pixel imaging via compressive sampling *IEEE Signal Process. Mag.* **25** 83–91
- [86] Coifman R, Geshwind F and Meyer Y 2001 Noiselets *Appl. Comput. Harmon. Anal.* **10** 27–44
- [87] Wu Y, Ye P, Mirza I O, Arce G R and Prather D W 2010 Experimental demonstration of an optical-sectioning compressive sensing microscope (CSM) *Opt. Express* **18** 24565
- [88] Liang M, Stehr R L and Krause A W 1997 Confocal pattern period in multiple-aperture confocal imaging systems with coherent illumination *Opt. Lett.* **22** 751
- [89] Cai X, Hu B, Sun T, Kelly K F and Baldelli S 2011 Sum frequency generation-compressive sensing microscope *J. Chem. Phys.* **135** 194202
- [90] Zhu L, Zhang W, Elnatan D and Huang B 2012 Faster STORM using compressed sensing *Nat. Methods* **9** 721–3
- [91] Huang J, Gumpfer K, Chi Y, Sun M and Ma J 2015 Fast 2D super-resolution image reconstruction algorithm for ultra-high emitter density *Opt. Lett.* **40** 2989
- [92] Studer V, Bobin J, Chahid M, Mousavi H S, Candes E and Dahan M 2012 Compressive fluorescence microscopy for biological and hyperspectral imaging *Proc. Natl Acad. Sci.* **109** E1679–87
- [93] Coskun A F, Sencan I, Su T-W and Ozcan A 2010 Lensless wide-field fluorescent imaging on a chip using compressive decoding of sparse objects *Opt. Express* **18** 10510–23
- [94] Sencan I, Coskun A F, Sikora U and Ozcan A 2014 Spectral Demultiplexing in holographic and fluorescent on-chip microscopy *Sci. Rep.* **4** 3760
- [95] Yang S, Lee J, Lee Y, Lee M and Lee B-U 2015 Estimation of multiexponential fluorescence decay parameters using compressive sensing *J. Biomed. Opt.* **20** 096003
- [96] Brady D J, Choi K, Marks D L, Horisaki R and Lim S 2009 Compressive holography *Opt. Express* **17** 13040–9
- [97] Denis L, Lorenz D, Thiébaud E, Fournier C and Trede D 2009 Inline hologram reconstruction with sparsity constraints *Opt. Lett.* **34** 3475
- [98] Cull C F, Millkner D A, Mait J N, Mattheiss M and Brady D J 2010 Millimeter-wave compressive holography *Appl. Opt.* **49** E67
- [99] Choi K, Horisaki R, Hahn J, Lim S, Marks D L, Schulz T J and Brady D J 2010 Compressive holography of diffuse objects *Appl. Opt.* **49** H1

- [100] Rivenson Y, Stern A and Javidi B 2010 Compressive Fresnel holography *J. Disp. Technol.* **6** 506–9
- [101] Zhang X and Lam E Y 2010 Edge-preserving sectional image reconstruction in optical scanning holography *J. Opt. Soc. Am. A* **27** 1630
- [102] Rivenson Y and Stern A 2011 Conditions for practicing compressive Fresnel holography *Opt. Lett.* **36** 3365
- [103] Rivenson Y, Stern A and Rosen J 2011 Compressive multiple view projection incoherent holography *Opt. Express* **19** 6109
- [104] Rivenson Y, Rot A, Balber S, Stern A and Rosen J 2012 Recovery of partially occluded objects by applying compressive Fresnel holography *Opt. Lett.* **37** 1757
- [105] Liu Y, Tian L, Lee J W, Huang H Y H, Triantafyllou M S and Barbastathis G 2012 Scanning-free compressive holography for object localization with subpixel accuracy *Opt. Lett.* **37** 3357
- [106] Rivenson Y, Stern A and Javidi B 2013 Overview of compressive sensing techniques applied in holography (Invited) *Appl. Opt.* **52** A423
- [107] Marim M M, Atlan M, Angelini E and Olivo-Marin J-C 2010 Compressed sensing with off-axis frequency-shifting holography *Opt. Lett.* **35** 871
- [108] Hahn J, Lim S, Choi K, Horisaki R and Brady D J 2011 Video-rate compressive holographic microscopic tomography *Opt. Express* **19** 7289
- [109] Rivenson Y, Stern A and Javidi B 2013 Improved depth resolution by single-exposure in-line compressive holography *Appl. Opt.* **52** A223
- [110] Liu X and Kang J U 2010 Compressive SD-OCT: the application of compressed sensing in spectral domain optical coherence tomography *Opt. Express* **18** 22010
- [111] Ashok A and Neifeld M A 2010 Compressive light field imaging *Proc. SPIE* **7690** 76900Q
- [112] Gabor D 1948 A new microscopic principle *Nature* **161** 777–8
- [113] Goodman J W 2000 *Statistical Optics* (New York: Wiley)
- [114] Harvey J E 1979 Fourier treatment of near-field scalar diffraction theory *Am. J. Phys.* **47** 974–80
- [115] Su T-W, Xue L and Ozcan A 2012 High-throughput lensfree 3D tracking of human sperms reveals rare statistics of helical trajectories *Proc. Natl Acad. Sci.* **109** 16018–22
- [116] Seo S, Isikman S O, Sencan I, Mudanyali O, Su T-W, Bishara W, Erlinger A and Ozcan A 2010 High-throughput lens-free blood analysis on a chip *Anal. Chem.* **82** 4621–7
- [117] Su T-W, Erlinger A, Tseng D and Ozcan A 2010 Compact and light-weight automated semen analysis platform using lensfree on-chip microscopy *Anal. Chem.* **82** 8307–12
- [118] Su T-W, Choi I, Feng J, Huang K, McLeod E and Ozcan A 2013 Sperm trajectories form chiral ribbons *Sci. Rep.* **3** 1664
- [119] Mudanyali O, Oztoprak C, Tseng D, Erlinger A and Ozcan A 2010 Detection of waterborne parasites using field-portable and cost-effective lensfree microscopy *Lab Chip* **10** 2419–23
- [120] Kesavan S V *et al* 2014 High-throughput monitoring of major cell functions by means of lensfree video microscopy *Sci. Rep.* **4** 5942
- [121] Huang K-W, Su T-W, Ozcan A and Chiou P-Y 2013 Optoelectronic tweezers integrated with lensfree holographic microscopy for wide-field interactive cell and particle manipulation on a chip *Lab Chip* **13** 2278–84
- [122] Ozcan A and Demirci U 2007 Ultra wide-field lens-free monitoring of cells on-chip *Lab Chip* **8** 98–106
- [123] Su T-W, Seo S, Erlinger A and Ozcan A 2009 High-throughput lensfree imaging and characterization of a heterogeneous cell solution on a chip *Biotechnol. Bioeng.* **102** 856–68
- [124] Pushkarsky I, Liu Y, Weaver W, Su T-W, Mudanyali O, Ozcan A and Di Carlo D 2014 Automated single-cell motility analysis on a chip using lensfree microscopy *Sci. Rep.* **4** 4717
- [125] Tsai H-F, Tsai Y-C, Yagur-Kroll S, Palevsky N, Belkin S and Cheng J-Y 2015 Water pollutant monitoring by a whole cell array through lens-free detection on CCD *Lab Chip* **15** 1472–80
- [126] Tanaka T, Sunaga Y, Hatakeyama K and Matsunaga T 2010 Single-cell detection using a thin film transistor photosensor with micro-partitions *Lab Chip* **10** 3348–54
- [127] Saeki T, Hosokawa M, Lim T, Harada M, Matsunaga T and Tanaka T 2014 Digital cell counting device integrated with a single-cell array *PLoS One* **9** e89011
- [128] Seo S, Su T-W, Tseng D K, Erlinger A and Ozcan A 2009 Lensfree holographic imaging for on-chip cytometry and diagnostics *Lab Chip* **9** 777–87
- [129] Stybayeva G, Mudanyali O, Seo S, Silangcrúz J, Macal M, Ramanculov E, Dandekar S, Erlinger A, Ozcan A and Revzin A 2010 Lensfree holographic imaging of antibody microarrays for high-throughput detection of leukocyte numbers and function *Anal. Chem.* **82** 3736–44
- [130] Tanaka T, Saeki T, Sunaga Y and Matsunaga T 2010 High-content analysis of single cells directly assembled on CMOS sensor based on color imaging *Biosens. Bioelectron.* **26** 1460–5
- [131] Zhang X, Khimji I, Gurkan U A, Safaee H, Catalano P N, Keles H O, Kayaalp E and Demirci U 2011 Lensless imaging for simultaneous microfluidic sperm monitoring and sorting *Lab Chip* **11** 2535–40
- [132] Moscelli N, van den Driesche S, Witarski W, Pastorekova S and Vellekoop M J 2011 An imaging system for real-time monitoring of adherently grown cells *Sensors Actuators* **172** 175–80
- [133] Kim S B, Bae H, Cha J M, Moon S J, Dokmeci M R, Cropek D M and Khademhosseini A 2011 A cell-based biosensor for real-time detection of cardiotoxicity using lensfree imaging *Lab Chip* **11** 1801–7
- [134] Jin G, Yoo I-H, Paek S P, Yang J-W, Ha U-H, Paek S-H and Seo S 2012 Lens-free shadow image based high-throughput continuous cell monitoring technique *Biosens. Bioelectron.* **38** 126–31
- [135] Dolega M E, Allier C, Vinjimore Kesavan S, Gerbaud S, Kermarrec F, Marcoux P, Dinten J-M, Gidrol X and Picollet-D'Hahan N 2013 Label-free analysis of prostate acini-like 3D structures by lensfree imaging *Biosens. Bioelectron.* **49** 176–83
- [136] Kwak Y H, Lee J, Lee J, Kwak S H, Oh S, Paek S-H, Ha U-H and Seo S 2014 A simple and low-cost biofilm quantification method using LED and CMOS image sensor *J. Microbiol. Methods* **107** 150–6
- [137] Penwill L A, Batten G E, Castagnetti S and Shaw A M 2014 Growth phenotype screening of *S. pombe* using a lensless microscope *Biosens. Bioelectron.* **54** 345–50
- [138] Musayev J, Altiner C, Adiguzel Y, Kulah H, Eminoglu S and Akin T 2014 Capturing and detection of MCF-7 breast cancer cells with a CMOS image sensor *Sensors Actuators* **215** 105–14
- [139] Roy M, Seo D, Oh C-H, Nam M-H, Kim Y J and Seo S 2015 Low-cost telemedicine device performing cell and particle size measurement based on lens-free shadow imaging technology *Biosens. Bioelectron.* **67** 715–23
- [140] Cui X, Lee L M, Heng X, Zhong W, Sternberg P W, Psaltis D and Yang C 2008 Lensless high-resolution on-chip optofluidic microscopes for *C. elegans* and cell imaging *Proc. Natl Acad. Sci.* **105** 10670–5
- [141] Lee L M, Cui X and Yang C 2009 The application of on-chip optofluidic microscopy for imaging *G. lamblia* trophozoites and cysts *Biomed. Microdevices* **11** 951–8
- [142] Pang S, Cui X, DeModena J, Wang Y M, Sternberg P and Yang C 2010 Implementation of a color-capable optofluidic microscope on a RGB CMOS color sensor chip substrate *Lab Chip* **10** 411–4

- [143] Bishara W, Zhu H and Ozcan A 2010 Holographic optofluidic microscopy *Opt. Express* **18** 27499
- [144] Isikman S O, Bishara W, Zhu H and Ozcan A 2011 Optofluidic tomography on a chip *Appl. Phys. Lett.* **98** 161109
- [145] Shanmugam A and Salthouse C 2014 Lensless fluorescence imaging with height calculation *J. Biomed. Opt.* **19** 016002
- [146] Martinelli L, Choumane H, Ha K-N, Sagarzazu G, Goutel C, Weisbuch C, Gacoin T and Benisty H 2007 Sensor-integrated fluorescent microarray for ultrahigh sensitivity direct-imaging bioassays: role of a high rejection of excitation light *Appl. Phys. Lett.* **91** 083901
- [147] Ah Lee S, Ou X, Lee J E and Yang C 2013 Chip-scale fluorescence microscope based on a silo-filter complementary metal-oxide semiconductor image sensor *Opt. Lett.* **38** 1817–9
- [148] Coskun A F, Sencan I, Su T-W and Ozcan A 2011 Lensfree fluorescent on-chip imaging of transgenic *C. elegans* over an ultra-wide field-of-view *PLoS One* **6** e15955
- [149] Coskun A F, Su T-W and Ozcan A 2010 Wide field-of-view lens-free fluorescent imaging on a chip *Lab Chip* **10** 824–7
- [150] Coskun A F, Sencan I, Su T-W and Ozcan A 2011 Wide-field lensless fluorescent microscopy using a tapered fiber-optic faceplate on a chip *Analyst* **136** 3512–8
- [151] Arpali S A, Arpali C, Coskun A F, Chiang H-H and Ozcan A 2012 High-throughput screening of large volumes of whole blood using structured illumination and fluorescent on-chip imaging *Lab Chip* **12** 4968–71
- [152] Lucy L B 1974 An iterative technique for the rectification of observed distributions *Astron. J.* **79** 745
- [153] Richardson W H 1972 Bayesian-based iterative method of image restoration *J. Opt. Soc. Am.* **62** 55
- [154] Han C, Pang S, Bower D V, Yiu P and Yang C 2013 Wide field-of-view on-chip talbot fluorescence microscopy for longitudinal cell culture monitoring from within the incubator *Anal. Chem.* **85** 2356–60
- [155] Reddington A P, Trueb J T, Freedman D S, Tuysuzoglu A, Daaboul G G, Lopez C A, Karl W C, Connor J H, Fawcett H and Unlu M S 2013 An Interferometric reflectance imaging sensor for point of care viral diagnostics *IEEE Trans. Biomed. Eng.* **60** 3276–83
- [156] Lee M, Yaglidere O and Ozcan A 2011 Field-portable reflection and transmission microscopy based on lensless holography *Biomed. Opt. Express* **2** 2721–30
- [157] Biener G, Greenbaum A, Isikman S O, Lee K, Tseng D and Ozcan A 2011 Combined reflection and transmission microscope for telemedicine applications in field settings *Lab Chip* **11** 2738–43
- [158] Hardie R C 1998 High-resolution image reconstruction from a sequence of rotated and translated frames and its application to an infrared imaging system *Opt. Eng.* **37** 247
- [159] Barron J L, Fleet D J, Beauchemin S S and Burkitt T A 1992 Performance of optical flow techniques *IEEE Computer Society Conf. on Computer Vision and Pattern Recognition* pp 236–42
- [160] Elad M and Hel-Or Y 2001 A fast super-resolution reconstruction algorithm for pure translational motion and common space-invariant blur *IEEE Trans. Image Process.* **10** 1187–93
- [161] Bishara W, Su T-W, Coskun A F and Ozcan A 2010 Lensfree on-chip microscopy over a wide field-of-view using pixel super-resolution *Opt. Express* **18** 11181–91
- [162] Bishara W, Sikora U, Mudanyali O, Su T-W, Yaglidere O, Luckhart S and Ozcan A 2011 Holographic pixel super-resolution in portable lensless on-chip microscopy using a fiber-optic array *Lab Chip* **11** 1276–9
- [163] Ashok A and Neifeld M A 2007 Pseudorandom phase masks for superresolution imaging from subpixel shifting *Appl. Opt.* **46** 2256
- [164] Greenbaum A, Luo W, Khademhosseini B, Su T-W, Coskun A F and Ozcan A 2013 Increased space-bandwidth product in pixel super-resolved lensfree on-chip microscopy *Sci. Rep.* **3** 1717
- [165] McLeod E, Luo W, Mudanyali O, Greenbaum A and Ozcan A 2013 Toward giga-pixel nanoscopy on a chip: a computational wide-field look at the nano-scale without the use of lenses *Lab Chip* **13** 2028–35
- [166] Greenbaum A, Luo W, Su T-W, Göröcs Z, Xue L, Isikman S O, Coskun A F, Mudanyali O and Ozcan A 2012 Imaging without lenses: achievements and remaining challenges of wide-field on-chip microscopy *Nat. Methods* **9** 889–95
- [167] Zheng G, Lee S A, Yang S and Yang C 2010 Sub-pixel resolving optofluidic microscope for on-chip cell imaging *Lab Chip* **10** 3125–9
- [168] Huang X, Guo J, Wang X, Yan M, Kang Y and Yu H 2014 A contact-imaging based microfluidic cytometer with machine-learning for single-frame super-resolution processing *PLoS One* **9** e104539
- [169] Zheng G, Lee S A, Antebi Y, Elowitz M B and Yang C 2011 The ePetri dish, an on-chip cell imaging platform based on subpixel perspective sweeping microscopy (SPSM) *Proc. Natl Acad. Sci.* **108** 16889–94
- [170] Lee S A, Zheng G, Mukherjee N and Yang C 2012 On-chip continuous monitoring of motile microorganisms on an ePetri platform *Lab Chip* **12** 2385–90
- [171] Lee S A, Erath J, Zheng G, Ou X, Willems P, Eichinger D, Rodriguez A and Yang C 2014 Imaging and identification of waterborne parasites using a chip-scale microscope *PLoS One* **9** e89712
- [172] Rayleigh L 1899 On the transmission of light through an atmosphere containing small particles in suspension, and on the origin of the blue of the sky *Phil. Mag. Ser.* **47** 375–84
- [173] Daaboul G G, Yurt A, Zhang X, Hwang G M, Goldberg B B and Ünlü M S 2010 High-throughput detection and sizing of individual low-index nanoparticles and viruses for pathogen identification *Nano Lett.* **10** 4727–31
- [174] Monroe M R, Daaboul G G, Tuysuzoglu A, Lopez C A, Little F F and Ünlü M S 2013 Single nanoparticle detection for multiplexed protein diagnostics with attomolar sensitivity in serum and unprocessed whole blood *Anal. Chem.* **85** 3698–706
- [175] Avci O, Ünlü N L, Özkumur A Y and Ünlü M S 2015 Interferometric reflectance imaging sensor (IRIS)—a platform technology for multiplexed diagnostics and digital detection *Sensors* **15** 17649–65
- [176] McLeod E and Ozcan A 2014 Nano-imaging enabled via self-assembly *Nano Today* **9** 560–73
- [177] Mudanyali O, Bishara W and Ozcan A 2011 Lensfree super-resolution holographic microscopy using wetting films on a chip *Opt. Express* **19** 17378–89
- [178] Mudanyali O, McLeod E, Luo W, Greenbaum A, Coskun A F, Hennequin Y, Allier C P and Ozcan A 2013 Wide-field optical detection of nanoparticles using on-chip microscopy and self-assembled nanolenses *Nat. Photon.* **7** 247–54
- [179] Allier C P, Hiernard G, Poher V and Dinten J M 2010 Bacteria detection with thin wetting film lensless imaging *Biomed. Opt. Express* **1** 762–70
- [180] Hennequin Y, Allier C P, McLeod E, Mudanyali O, Migliozi D, Ozcan A and Dinten J-M 2013 Optical detection and sizing of single nanoparticles using continuous wetting films *ACS Nano* **7** 7601–9

- [181] McLeod E, Nguyen C, Huang P, Luo W, Veli M and Ozcan A 2014 Tunable vapor-condensed nanolenses *ACS Nano* **8** 7340–9
- [182] McLeod E, Dincer T U, Veli M, Ertas Y N, Nguyen C, Luo W, Greenbaum A, Feizi A and Ozcan A 2015 High-throughput and label-free single nanoparticle sizing based on time-resolved on-chip microscopy *ACS Nano* **9** 3265–73
- [183] Berne B J and Pecora R 2000 *Dynamic Light Scattering: With Applications to Chemistry, Biology, and Physics* (New York: Dover)
- [184] Filipe V, Hawe A and Jiskoot W 2010 Critical evaluation of nanoparticle tracking analysis (NTA) by nanosight for the measurement of nanoparticles and protein aggregates *Pharm. Res.* **27** 796–810
- [185] Göröcs Z, McLeod E and Ozcan A 2015 Enhanced light collection in fluorescence microscopy using self-assembled micro-reflectors *Sci. Rep.* **5** 10999
- [186] Isikman S O, Bishara W, Mavandadi S, Yu F W, Feng S, Lau R and Ozcan A 2011 Lens-free optical tomographic microscope with a large imaging volume on a chip *Proc. Natl Acad. Sci.* **108** 7296–301
- [187] Isikman S O, Bishara W and Ozcan A 2011 Partially coherent lensfree tomographic microscopy (invited) *Appl. Opt.* **50** H253
- [188] Meng H and Hussain F 1995 In-line recording and off-axis viewing technique for holographic particle velocimetry *Appl. Opt.* **34** 1827
- [189] Su T-W, Isikman S O, Bishara W, Tseng D, Erlinger A and Ozcan A 2010 Multi-angle lensless digital holography for depth resolved imaging on a chip *Opt. Express* **18** 9690
- [190] Brooks R A and Di Chiro G 1975 Theory of image reconstruction in computed tomography *Radiology* **117** 561–72
- [191] Isikman S O, Greenbaum A, Luo W, Coskun A F and Ozcan A 2012 Giga-pixel lensfree holographic microscopy and tomography using color image sensors *PLoS One* **7** e45044
- [192] Reed Teague M 1983 Deterministic phase retrieval: a green's function solution *J. Opt. Soc. Am.* **73** 1434
- [193] Waller L, Tian L and Barbastathis G 2010 Transport of Intensity imaging with higher order derivatives *Opt. Express* **18** 12552
- [194] Gerchberg R and Saxton O 1972 A practical algorithm for the determination of the phase from image and diffraction plane pictures *Optik* **35** 237–46
- [195] Mudanyali O, Tseng D, Oh C, Isikman S O, Sencan I, Bishara W, Oztoprak C, Seo S, Khademhosseini B and Ozcan A 2010 Compact, light-weight and cost-effective microscope based on lensless incoherent holography for telemedicine applications *Lab Chip* **10** 1417–28
- [196] Greenbaum A and Ozcan A 2012 Maskless imaging of dense samples using pixel super-resolution based multi-height lensfree on-chip microscopy *Opt. Express* **20** 3129–43
- [197] Greenbaum A, Sikora U and Ozcan A 2012 Field-portable wide-field microscopy of dense samples using multi-height pixel super-resolution based lensfree imaging *Lab Chip* **12** 1242–5
- [198] Greenbaum A, Zhang Y, Feizi A, Chung P-L, Luo W, Kandukuri S R and Ozcan A 2014 Wide-field computational imaging of pathology slides using lens-free on-chip microscopy *Sci. Transl. Med.* **6** 267ra175
- [199] Weidling J, Isikman S O, Greenbaum A, Ozcan A and Botvinick E 2012 Lens-free computational imaging of capillary morphogenesis within 3D substrates *J. Biomed. Opt.* **17** 126018
- [200] Greenbaum A, Feizi A, Akbari N and Ozcan A 2013 Wide-field computational color imaging using pixel super-resolved on-chip microscopy *Opt. Express* **21** 12469–83
- [201] Greenbaum A, Akbari N, Feizi A, Luo W and Ozcan A 2013 Field-portable pixel super-resolution colour microscope *PLoS One* **8** e76475
- [202] Göröcs Z, Orzó L, Kiss M, Tóth V and Tőkés S 2010 In-line color digital holographic microscope for water quality measurements ed M Kinnunen and R Myllylä *Proc. SPIE* **7376** 737614
- [203] Isikman S O, Sencan I, Mudanyali O, Bishara W, Oztoprak C and Ozcan A 2010 Color and monochrome lensless on-chip imaging of *C. elegans* over a wide field-of-view *Lab Chip* **10** 1109
- [204] Dijkstra E W 1959 A note on two problems in connexion with graphs *Numer. Math.* **1** 269–71
- [205] Wei Q, McLeod E, Qi H, Wan Z, Sun R and Ozcan A 2013 On-chip cytometry using plasmonic nanoparticle enhanced lensfree holography *Sci. Rep.* **3** 1699
- [206] Arlett J L, Myers E B and Roukes M L 2011 Comparative advantages of mechanical biosensors *Nat. Nanotechnol.* **6** 203–15
- [207] Su J, Goldberg A F G and Stoltz B 2016 Label-free detection of single nanoparticles and biological molecules using microtoroid optical resonators *Light Sci. Appl.* **5** e16001
- [208] Su J 2015 Label-free single exosome detection using frequency-locked microtoroid optical resonators *ACS Photonics* **2** 1241–5
- [209] Ebbesen T W, Lezec H J, Ghaemi H F, Thio T and Wolff P A 1998 Extraordinary optical transmission through sub-wavelength hole arrays *Nature* **391** 667–9
- [210] Rindzevicius T, Alaverdyan Y, Dahlin A, Höök F, Sutherland D S and Käll M 2005 Plasmonic sensing characteristics of single nanometric holes *Nano Lett.* **5** 2335–9
- [211] Khademhosseini B, Biener G, Sencan I, Su T-W, Coskun A F and Ozcan A 2010 Lensfree sensing on a microfluidic chip using plasmonic nanoapertures *Appl. Phys. Lett.* **97** 221107
- [212] Cetin A E, Coskun A F, Galarreta B C, Huang M, Herman D, Ozcan A and Altug H 2014 Handheld high-throughput plasmonic biosensor using computational on-chip imaging *Light Sci. Appl.* **3** e122
- [213] Coskun A F, Cetin A E, Galarreta B C, Alvarez D A, Altug H and Ozcan A 2014 Lensfree optofluidic plasmonic sensor for real-time and label-free monitoring of molecular binding events over a wide field-of-view *Sci. Rep.* **4** 6789
- [214] Bourquin Y, Reboud J, Wilson R, Zhang Y and Cooper J M 2011 Integrated immunoassay using tuneable surface acoustic waves and lensfree detection *Lab Chip* **11** 2725–30
- [215] Colle F, Vercautse D, Peeters S, Liu C, Stakenborg T, Lagae L and Del-Favero J 2013 Lens-free imaging of magnetic particles in DNA assays *Lab Chip* **13** 4257–62
- [216] Gorocs Z and Ozcan A 2013 On-chip biomedical imaging *IEEE Rev. Biomed. Eng.* **6** 29–46
- [217] Bishara W, Sikora U, Mudanyali O, Su T-W, Yaglidere O, Luckhart S and Ozcan A 2011 Handheld, lensless microscope identifies malaria parasites *SPIE Newsroom* (DOI: 10.1117/2.1201107.003812)
- [218] McLeod E, Wei Q and Ozcan A 2015 Democratization of nanoscale imaging and sensing tools using photonics *Anal. Chem.* **87** 6434–45
- [219] Zhu H, Yaglidere O, Su T-W, Tseng D and Ozcan A 2011 Cost-effective and compact wide-field fluorescent imaging on a cell-phone *Lab Chip* **11** 315–22
- [220] Zhu H, Sencan I, Wong J, Dimitrov S, Tseng D, Nagashima K and Ozcan A 2013 Cost-effective and rapid blood analysis on a cell-phone *Lab Chip* **13** 1282–8
- [221] Ludwig S K J, Zhu H, Phillips S, Shiledar A, Feng S, Tseng D, van Ginkel L A, Nielsen M W F and Ozcan A

- 2014 Cellphone-based detection platform for rbST biomarker analysis in milk extracts using a microsphere fluorescence immunoassay *Anal. Bioanal. Chem.* **406** 6857–66
- [222] Wei Q *et al* 2013 Fluorescent imaging of single nanoparticles and viruses on a smart phone *ACS Nano* **7** 9147–55
- [223] Wei Q *et al* 2014 Imaging and sizing of single DNA molecules on a mobile phone *ACS Nano* **8** 12725–33
- [224] Koydemir H C, Gorocs Z, Tseng D, Cortazar B, Feng S, Chan R Y L, Burbano J, McLeod E and Ozcan A 2015 Rapid imaging, detection and quantification of *G. lamblia* cysts using mobile-phone based fluorescent microscopy and machine learning *Lab Chip* **15** 1284–93
- [225] Breslauer D N, Maamari R N, Switz N A, Lam W A and Fletcher D A 2009 Mobile phone based clinical microscopy for global health applications *PLoS One* **4** e6320
- [226] Switz N A, D'Ambrosio M V and Fletcher D A 2014 Low-cost mobile phone microscopy with a reversed mobile phone camera lens *PLoS One* **9** e95330
- [227] Chang J, Arbeláez P, Switz N, Reber C, Tapley A, Davis J L, Cattamanchi A, Fletcher D and Malik J 2012 Automated tuberculosis diagnosis using fluorescence images from a mobile microscope *Medical Image Computing and Computer-Assisted Intervention ... Int. Conf. on Medical Image Computing and Computer-Assisted Intervention* vol 15 pp 345–52
- [228] Tapley A, Switz N, Reber C, Davis J L, Miller C, Matovu J B, Worodria W, Huang L, Fletcher D A and Cattamanchi A 2013 Mobile digital fluorescence microscopy for diagnosis of tuberculosis *J. Clin. Microbiol.* **51** 1774–8
- [229] Chaisson L H *et al* 2015 Evaluation of mobile digital light-emitting diode fluorescence microscopy in Hanoi, Viet Nam *Int. J. Tuberc. Lung Dis.* **19** 1068–72
- [230] Ephraim R K D, Duah E, Cybulski J S, Prakash M, D'Ambrosio M V, Fletcher D A, Keiser J, Andrews J R and Bogoch I I 2015 Diagnosis of schistosoma haematobium infection with a mobile phone-mounted foldscope and a reversed-lens cellscope in Ghana *Am. J. Trop. Med. Hyg.* **92** 1253–6
- [231] D'Ambrosio M V *et al* 2015 Point-of-care quantification of blood-borne filarial parasites with a mobile phone microscope *Sci. Transl. Med.* **7** 286re4
- [232] Maamari R N, Keenan J D, Fletcher D A and Margolis T P 2014 A mobile phone-based retinal camera for portable wide field imaging *Br. J. Ophthalmol.* **98** 438–41
- [233] Maamari R N, Ausayakhun S, Margolis T P, Fletcher D A and Keenan J D 2014 Novel telemedicine device for diagnosis of corneal abrasions and ulcers in resource-poor settings *JAMA Ophthalmol.* **132** 894–5
- [234] Skandarajah A, Reber C D, Switz N A and Fletcher D A 2014 Quantitative imaging with a mobile phone microscope *PLoS One* **9** e96906
- [235] Cybulski J S, Clements J and Prakash M 2014 Foldscope: origami-based paper microscope *PLoS One* **9** e98781
- [236] Phillips Z F, D'Ambrosio M V, Tian L, Rulison J J, Patel H S, Sadras N, Gande A V, Switz N A, Fletcher D A and Waller L 2015 Multi-contrast imaging and digital refocusing on a mobile microscope with a domed LED array *PLoS One* **10** e0124938
- [237] Tseng D, Mudanyali O, Oztoprak C, Isikman S O, Sencan I, Yaglidere O and Ozcan A 2010 Lensfree microscopy on a cellphone *Lab Chip* **10** 1787–92
- [238] Navruz I, Coskun A F, Wong J, Mohammad S, Tseng D, Nagi R, Phillips S and Ozcan A 2013 Smart-phone based computational microscopy using multi-frame contact imaging on a fiber-optic array *Lab Chip* **13** 4015–23
- [239] Isikman S O, Bishara W, Sikora U, Yaglidere O, Yeah J and Ozcan A 2011 Field-portable lensfree tomographic microscope *Lab Chip* **11** 2222–30
- [240] Kesavan S V, Navarro F P, Menneteau M, Mittler F, David-Watine B, Dubrulle N, Shorte S L, Chalmond B, Dinten J-M and Allier C P 2014 Real-time label-free detection of dividing cells by means of lensfree video-microscopy *J. Biomed. Opt.* **19** 036004
- [241] Lee S A, Leitao R, Zheng G, Yang S, Rodriguez A and Yang C 2011 Color capable sub-pixel resolving optofluidic microscope and its application to blood cell imaging for malaria diagnosis *PLoS One* **6** e26127
- [242] Koydemir H C, Bogoch I I, Tseng D, Ephraim R K D, Duah E, Tee J, Andrews J R and Ozcan A 2016 Field-testing of a cost-effective mobile-phone based microscope for screening of *Schistosoma haematobium* *SPIE Photonics West Conf. Proc.* vol 9699 p 23